Real-time small-angle x-ray scattering study of the early stage of phase separation in the SiO_2-BaO-K_2O system

G. Brian Stephenson
IBM Research Division, P.O. Box 218, Yorktown Heights, New York 10598

William K. Warburton
X-ray Instrumentation Associates, 1300 Mills Street, Menlo Park, California 94025

Wolfgang Haller
National Institute of Standards and Technology, Gaithersburg, Maryland 20899

Arthur Bienenstock
Stanford Synchrotron Radiation Laboratory, Bin 69, P.O. Box 4349, Stanford, California 94309
(Received 27 December 1989; revised manuscript received 15 November 1990)

Time-resolved small-angle x-ray scattering was used to study the early stage of phase separation in a silicate system. Scattering patterns were acquired in real time as a sample was quenched *in situ* from a temperature T_1 in the single-phase region directly to a temperature T_2 in the two-phase region and held isothermally. This was made possible by using a high-intensity synchrotron x-ray source, a fast position-sensitive detector, a sample heater capable of rapid quenches, and a sample composition chosen to give good scattering contrast and relatively slow kinetics. The composition studied, 90 mol % SiO_2, 5 mol % BaO, and 5 mol % K_2O, undergoes subliquidus phase separation at temperatures below 1021 K to form alkali-oxide-rich and alkali-oxide-poor amorphous phases. The temperatures used were $T_1 = 1074$ K and $T_2 = 1014$, 995, 970, and 950 K. While the resultant data agree qualitatively with the linearized thermodynamics of the Cahn-Hilliard-Cook (CHC) theory of spinodal decomposition (i.e., the structure factor changes exponentially with time at each wave number), they do not agree with the simple diffusive kinetics used in the CHC theory. The data are in very good agreement with a modified theory incorporating diffusion-induced-flow (DIF) kinetics, in which one considers both the generation of stress arising from unequal mobilities of the diffusing species and the relaxation of this stress through deformation. Values of the material parameters as a function of temperature obtained from fits of the DIF theory to the data are in reasonable agreement with independent measurements and estimates based on a regular-solution model. For amorphous systems in particular, these results provide direct evidence that viscous flow is the rate-limiting step for the interdiffusion of network-forming and network-modifying species over the short length scales involved in the early stage of phase separation.

I. INTRODUCTION

According to classical theory, the phase-separation process can be conceptually divided into an early stage and a late stage. In the early stage, an initially single-phase system transforms into a system consisting of relatively small regions of two phases having nearly equilibrium compositions. In the late stage, the average size of the regions in the two-phase system increases through a coarsening process. The early stage is driven by the bulk free-energy difference between the initial and final phases, while the late stage is driven by the free energy of the interfaces generated during the early stage. Two qualitatively different limiting cases for the mechanism of early-stage phase separation have been distinguished:[1] nucleation and growth for metastable initial states and spinodal decomposition for unstable initial states. Spinodal decomposition theory is especially interesting, because it is based directly on the concept of the thermodynamic driving force for diffusion originally developed for interdiffusion in nonideal single-phase systems.[2] Comparison of theory and experiment on the kinetics of the early stage of phase separation in the unstable region of the phase diagram thus tests our fundamental understanding of interdiffusion in the single-phase region.

Over the past two decades, there have been many small-angle x-ray- and neutron-scattering studies of both early- and late-stage phase-separation behavior in the unstable region of glass-forming oxide systems.[13–18] The motivation for these studies has been not only the technological importance of phase separation in silicate and borate glasses, but also the belief that such systems can serve as simple experimental models to test basic theory. Diffusion coefficients in glass-forming systems can be much smaller than those in typical liquids, so that phase separation proceeds at a rate more accessible to experiment. In addition, the classical distinctions between metastability and instability, and between the early and late

stages of phase separation, are expected to be most valid for systems which have long-range interactions between molecules.[19–22] Since glass-forming oxides, like polymers, are expected to have relatively long-range interactions,[17] they provide a good test of classical theory. Although the more recent experimental results for the late stage of phase separation[11,15,16,18] agree well with a generalized coarsening theory based on dynamic scaling, results for the early stage of phase separation[4–8,11–13,17] are only qualitatively consistent with classical Cahn-Hilliard-Cook (CHC) spinodal decomposition theory[1,23] and nonlinear extensions to it.[19,22,24] The quantitative agreement is so poor that theoretical and experimental structure factors have not been directly compared in any of these early-stage studies. These results have not provided a definitive test of spinodal decomposition theory because the observed discrepancies could always be attributed to experimental complications, such as an initial quench to and reheat from room temperature.

With the availability of intense synchrotron x-ray sources and advances in position-sensitive detector technology for time-resolved studies, we recognized an opportunity to carry out a small-angle-scattering study of the early stage of phase separation which avoids most of the experimental uncertainties of previous work on amorphous oxide systems. In particular, we have been able to measure the evolution of the structure factor in real time as a sample, initially at equilibrium *in situ* at a temperature T_1 in the single-phase region, is quenched directly to a temperature T_2 in the two-phase region and held isothermally. The composition studied, 90 mol% SiO_2, 5 mol% BaO, and 5 mol% K_2O, is chosen to have a sufficiently slow phase-separation rate and to give observable scattering at the earliest stage of phase separation. Since the sample is quenched directly from an equilibrium state, the initial state for the transition is better characterized than in previous work. The depth of the direct quenches $T_1 - T_2$ is relatively small, which minimizes complications such as phase separation during the quench and structural relaxation. The measurements are made using final temperatures T_2 in a range from just above to well within the unstable region. This range spans both sides of the maximum in phase-separation rate which arises from the trade-off between driving force and mobility. The ability to use direct quenches allows the study of the high-temperature, driving-force-limited side of the trade-off region, which previously was experimentally inaccessible. The measurement of the kinetics of reequilibration of small composition fluctuations in the metastable region above the unstable region also provides an important test of spinodal decomposition theory.

An initial analysis[25] of the experimental results of this study has shown that, although some general features of the CHC theory describe the observed behavior accurately, the shapes of CHC structure factors differ markedly from those measured. This discrepancy is not of the type attributable to nonlinear effects or late-stage scaling behavior. Instead, the wave-number dependence of the rate of change of the measured structure factor indicates that the rate-limiting step for composition change is of relaxational rather than diffusive nature. This conclusion has motivated the development of a model for interdiffusion,[26–28] which we will call the "diffusion-induced-flow" (DIF) theory. In DIF theory, one considers both the generation of stress owing to unequal mobilities of the diffusing species and the relaxation of this stress through deformation. For systems in which the species have very different mobilities (e.g., glass-forming oxides), DIF theory predicts that deformation is the rate-limiting step for interdiffusion over short length scales. This has significant consequences not only for spinodal decomposition, but also for any process involving interdiffusion. In this article, we present and analyze the experimental work which underlies these new theoretical developments. The experimental technique (described in detail in Ref. 25) is presented in Sec. II. The results are then compared in Sec. III with both the standard CHC theory and the linearized form of the DIF spinodal decomposition theory. In Sec. IV the agreement found between the DIF theory and the experimental data is evaluated by comparing the parameter values obtained to independent estimates.

II. X-RAY SCATTERING MEASUREMENTS

To carry out this time-resolved small-angle x-ray-scattering study of the early stage of phase separation using *in situ* quenches directly from the single-phase region, four coupled experimental innovations were required: (a) the use of a high-intensity synchrotron source, (b) the development of a fast position-sensitive detector, (c) the construction of a sample heater capable of fast quenches, and (d) the identification of a sample composition with a maximum rate of phase separation which is sufficiently slow. This maximum phase-separation rate must be slow relative to the time scales of both the quench and the scattering measurement. The time resolution of the scattering measurement is, in turn, determined by the scattering efficiency of the sample and the incident x-ray intensity, assuming that the detector system is fast enough. Scattering efficiency is proportional to the square of the density difference between the two incipient phases. The dual requirements of a low enough phase-separation rate and a high enough density difference significantly restricted the choice of sample compositions which could be used in the present study. The development of higher-intensity x-ray sources, coupled with faster detectors and *in situ* quenching techniques, promises much greater freedom in the choice of systems in future studies.

A. Choice of sample composition

Immiscibility between alkali-oxide-rich and alkali-oxide-poor amorphous phases has been found to occur in the glass-forming regions of almost all alkali-metal and alkaline-earth silicate and borate systems.[29] In several silicate systems (such as that studied here), the immiscibility occurs at temperatures below the equilibrium liquidus, where the amorphous phase is metastable with respect to crystallization; however, this crystallization is typically very slow relative to phase separation within the

amorphous phase. These systems are attractive for the present work because their atomic structure and phase diagrams are relatively well understood: The alkali-metal or alkaline-earth oxides act as "modifiers" in a network structure formed by the SiO_2 or B_2O_3. Since none of the binary systems have the optimum combination of phase-separation rate and density difference, it was necessary to use a composition in a ternary system. A typical ternary phase diagram of two modifiers in a silicate system is simple: An immiscibility surface extends across the silica corner to join the miscibility gaps of the limiting binaries. The critical temperature along the top of this surface varies from that of one limiting binary to that of the other, and the tie lines in the two-phase coexistence region below the surface radiate from the silica corner. Since atomic mobilities are strong functions of temperature, the maximum phase-separation rate depends strongly on the critical temperature. Thus, by choosing an appropriate ternary composition, a pseudobinary system with the desired phase-separation rate can be obtained.

Sample compositions in the SiO_2-BaO-K_2O system were used in this study. The subliquids immiscibility surface of this system is shown in Fig. 1 plotted in terms of oxide mole fraction x. This diagram is an interpolation of measurements using a pseudobinary regular solution (mean-field) model.[25,30–33] (This model is discussed further in the Appendix.) As Fig. 1 indicates, the ternary system can be approximated as a series of pseudobinary systems, each having a fixed modifier ratio $x_{BaO}/(x_{BaO}+x_{K_2O})$. The composition in any of these pseudobinary systems can be expressed as the total modifier mole fraction, $c \equiv x_{BaO}+x_{K_2O}$. Figure 2 shows the pseudobinary section with equal mole fractions of BaO and K_2O. The solid line in this diagram is the equilibrium coexistence boundary, and the dashed line is the spinodal calculated from the mean-field model. The composition in this section is given by

$$(SiO_2)_{1-c}(\tfrac{1}{2}BaO\cdot\tfrac{1}{2}K_2O)_c \ . \tag{1}$$

The critical point is calculated to be $T_c \simeq 1042$ K at $c \simeq 0.074$.

One complication which could arise with a ternary system is the possibility that two independent composition variables would be important in the phase-separation process, so that binary-system models would not apply. Even when the equilibrium phase diagram is pseudobinary, during phase separation the local composition could in general take on values which are not in the pseudobinary section if the mobilities or partial molal volumes of the diffusing species differ.[28] The conditions under which these complications arise during spinodal decomposition in ternary systems have been previously considered.[34] For the system studied here, such complications are not expected to be significant, since the thermodynamic tendency of the modifier cations Ba and K is to remain mixed at all temperatures, and the rate-limiting mobility for Ba-K mixing is orders of magnitude larger than that for (BaO·K_2O)-SiO_2 unmixing.[28,35] Thus spatial fluctuations in the modifier ratio $x_{BaO}/(x_{BaO}+x_{K_2O})$ will remain small, and the local composition can be described by the single composition variable c.

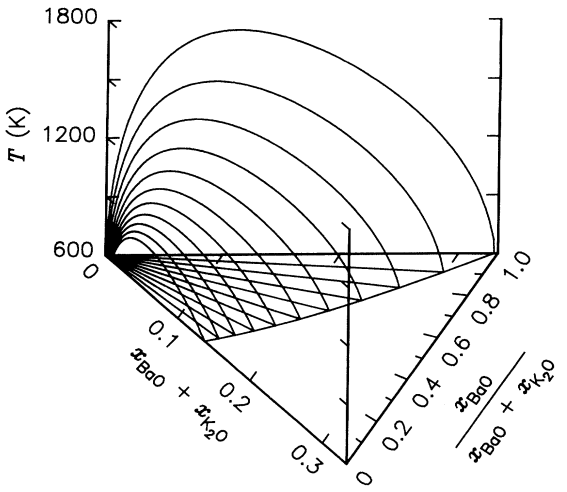

FIG. 1. Calculated phase diagram for the SiO_2-BaO-K_2O system, showing pseudobinary immiscibility with tie lines radiating from the silica corner.

Samples with compositions in the pseudobinary section shown in Fig. 2 were prepared at the National Bureau of Standards (now, Institute of Standards and Technology).[25] Difficulties were encountered in making homogeneous samples near the critical composition because of the high viscosity of the melt. Homogeneous samples

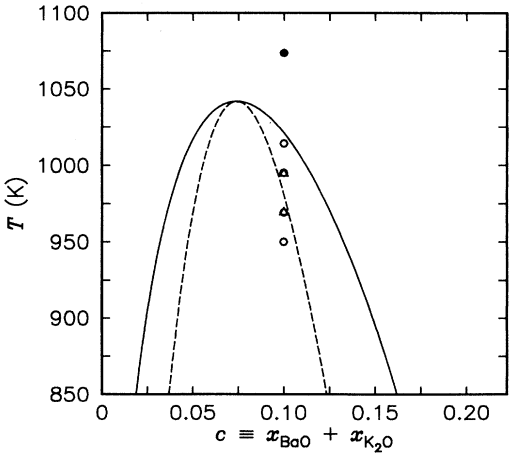

FIG. 2. Calculated phase diagram for the pseudobinary system $(SiO_2)_{1-c}(\frac{1}{2}BaO\cdot\frac{1}{2}K_2O)_c$, showing subliquidus immiscibility between two amorphous phases. Solid line: equilibrium two-phase coexistence boundary. Dashed line: mean-field spinodal calculated from regular solution model. Solid symbol: temperature T_1 of anneal in the single-phase region. Open symbols: temperatures T_2 of phase-separation runs in the two-phase region.

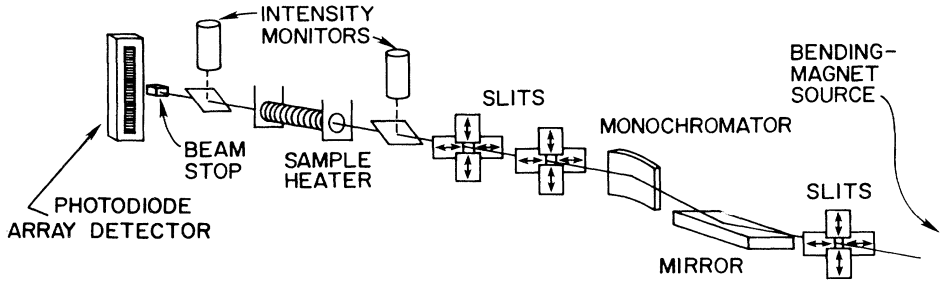

FIG. 3. Schematic of small-angle x-ray-scattering apparatus used at SSRL Beamline I-4 (not to scale).

were successfully made of compositions $c=0.10$ and 0.12; the composition $c=0.10$ was used in the study of phase-separation kinetics reported here. For the small-angle x-ray-scattering measurements, thin plates were cut and polished to a thickness of ~ 0.01 cm, corresponding to approximately one absorption length at the x-ray energy used.

B. Experimental procedure

The small-angle x-ray-scattering measurements were carried out at Beamline I-4 at the Stanford Synchrotron Radiation Laboratory (SSRL). The experimental geometry is shown schematically in Fig. 3. Radiation from the bending-magnet source was focused in the vertical by a mirror and in the horizontal by a bent Si(111) monochromator[36] tuned to a photon energy of 8.78 keV ($\lambda=1.41$ Å). Two sets of slits were used to define and collimate the incident beam. Two scintillation counters monitored the total intensity incident on and transmitted by the sample, respectively. These monitors and the position-sensitive detector were calibrated against an ion chamber, allowing the scattering measurements to be put on an absolute basis with $\pm 25\%$ accuracy. For typical storage-ring conditions (3.0 GeV, 85 mA), an incident intensity of 2.5×10^9 photons per second was obtained. A linear position-sensitive detector system based on a photodiode-array sensor was designed and built for these experiments so that complete small-angle x-ray-scattering patterns could be acquired within seconds.[25] The photodiode array operated as an integrating detector rather than a photon counter. The noise level of the detector (corresponding to ~ 2.6 photons per diode per scan) was sufficiently low that the Poisson statistics of the incoming photons was the dominant source of noise in the data.

The sample heater consisted of a miniature tube furnace, designed to hold the sample in the x-ray beam at a controlled temperature up to 1200 K and allow the temperature to be changed rapidly. A schematic of the heater is shown in Fig. 4. A water-cooled housing enclosed a heater assembly with a dry nitrogen atmosphere. The thin sample was heated primarily by thermal radiation at the temperatures used. Temperature gradients in the sample were minimized by the long aspect ratio of the tube furnace, since a uniformly hot surface enclosed at least 98% of the solid angle seen by any point on the sample. A thermocouple made of very fine wire was used to measure the sample temperature. Temperature nonuniformity in the sample region was measured to be ± 1 K. The temperature could be changed by 100 K with a time constant of about 10 sec by abruptly changing the voltage to the heater; after 100 sec the temperature stabilized to within ± 0.5 K for the duration of each run.

Scattering data were acquired in "runs" in which a sample was first equilibrated *in situ* at a temperature T_1 in the single-phase region and then quenched to a temperature T_2 in the two-phase region and isothermally held. The evolution of the structure factor was measured by recording a series of consecutive scattering patterns as phase separation occurred. In order to characterize the initial single-phase state of the sample, this series was started so that four patterns were recorded before the quench. For a typical run, 100 consecutive scattering patterns were recorded, each integrating over a 30.72-sec interval. Some runs were truncated owing to synchrotron beam loss. The same initial temperature $T_1=1074$ K was used in all runs. Four final temperatures T_2 were investigated; two were repeated to verify reproducibility. The runs are labeled $A-F$ in the order in which they were conducted. Temperatures T_1 and T_2 used in all runs are shown in the phase diagram in Fig. 2 as solid and open symbols, respectively. The same sample could be used in more than one run, since the anneal at T_1 reequilibrated

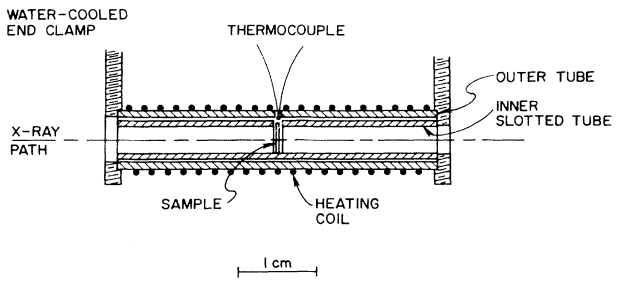

FIG. 4. Schematic of sample heater for time-resolved small-angle x-ray scattering.

the sample to a single-phase state each time. One sample was used to runs $A-C$; a second sample was used in runs $D-F$.

To determine appropriate conditions for the anneal in the single-phase region, several exploratory measurements were made in which the scattering was observed as the temperature of the sample was stepped upward and downward. The phase boundary was found to be at about 1020 K, and the time constant for dissolution of a two-phase structure was observed to be less than 1 min at 1074 K. The typical anneal for each run was therefore chosen to be 420 sec at 1074 K. To determine whether an anneal of this length would initiate crystallization, the evolution of the scattering during a 1310-sec anneal time was investigated in run B. During this long anneal, the scattering was recorded in a separate sequence of patterns with 12-sec resolution. (Since this data set is used in the analysis described below, we will refer to it as "run Z.") The scattering from the initial phase separation disappeared within about 60 sec, and no further change was observed during the anneal.

C. Data reduction

Since the "parasitic" scattering from slit edges, windows, air, etc., was a significant contribution to the total signal, it was measured for each run and subtracted after appropriate normalization. Figure 5 shows five scattering patterns measured at various times during run A, expressed as nominal cross section per unit volume (uncorrected for instrumental resolution). As in all data reported here, the time given for each pattern is the center of the time interval over which it was recorded, relative to the time of the initiation of the quench into the two-phase region. The pattern measured 77 sec before the quench is typical of the low-intensity, relatively uniform scattering from equilibrium composition fluctuations in the sample at the initial temperature T_1 in the single-phase region. The evolution of the uncorrected intensity as a function of time at various nominal scattering angles

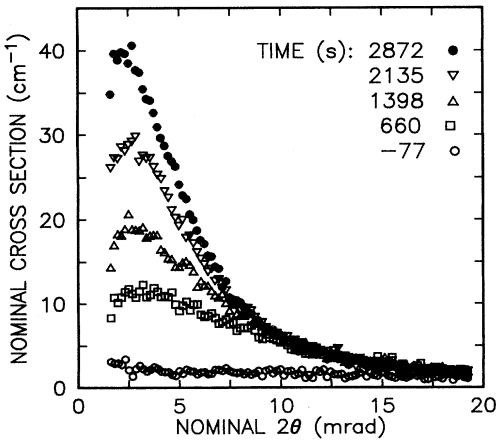

FIG. 5. Uncorrected scattering cross section per unit volume as a function of angle at several times during run A.

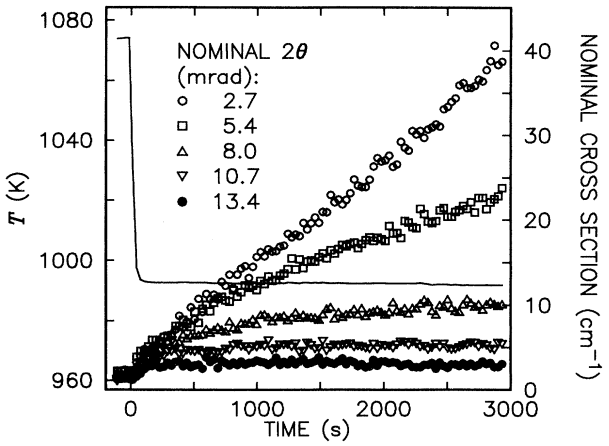

FIG. 6. Temperature (solid line) and uncorrected cross section per unit volume as a function of time at several angles, from run A.

is shown in Fig. 6 for run A. The sample temperature as a function of time is also plotted, showing the direct quench from the single-phase region. The equilibration time of this temperature profile is typical of all the phase-separation runs. At all except for the highest angles, most of the change in the scattering occurs at constant temperature.

For comparison with theory, every four consecutive scattering patterns were averaged together to produce patterns integrated over ~123 sec. Figure 7 shows the first such averaged pattern for each run $A-F$, as well as the average of the last half of run Z. These patterns were all measured before the quench with the sample equilibrated in the single-phase state at T_1. At angles larger

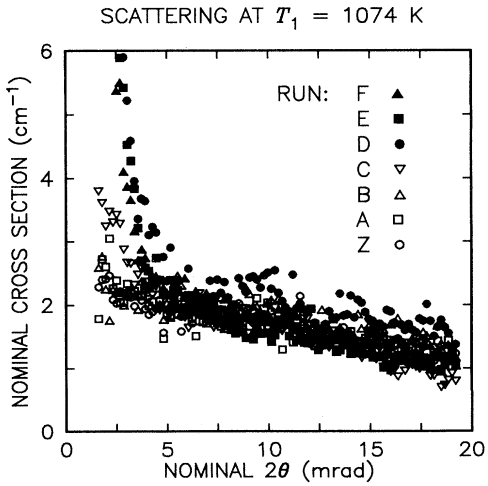

FIG. 7. Uncorrected scattering cross section per unit volume as a function of angle measured with the sample equilibrated at 1074 K, from all runs. Note that some points at low angle from runs $D-F$ are off scale.

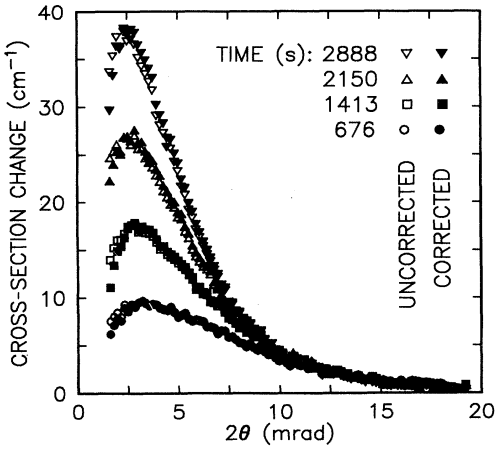

FIG. 8. Corrected and uncorrected scattering cross section change as a function of angle at several times during run *A*. Open symbols: uncorrected (as measured). Solid symbols: after correction for instrumental resolution.

than $2\theta \simeq 5$ mrad, all the measurements agree well. However, the sharp peak at zero angle due to parasitic scattering was not always completely removed by the subtraction procedure mentioned above. This was most apparent in runs $D-F$, because the sample did not completely span the opening in the heater. Since this peak appeared in the data recorded both before and after the quench and was constant in time, the measured quantity least affected by inaccuracy in the parasitic subtraction was the *change* in the scattering as a function of time. Therefore, for each run $A-F$, the quantity used for comparison with theory was the difference between the scattering measured during phase separation and the scattering from the single-phase sample measured before the quench shown in Fig. 7. The scattering measured during run Z (for which the accuracy of parasitic subtraction was relatively good) was used to characterize the single-phase reference state employed in all phase-separation runs.

To obtain the true differential scattering cross section per unit volume $d\sigma_V/d\Omega$ as a function of scattering angle 2θ, the instrumental resolution was deconvoluted from the measured patterns. The effect of this "slit-height" correction on the shape of typical scattering patterns is shown in Fig. 8.

III. ANALYSIS OF RESULTS

In this section we present analyses of our measurements using both the classical CHC theory and the linearized form of the DIF spinodal decomposition theory. Since the CHC theory is one limiting case of the linearized DIF theory, the formulation developed for DIF theory[28] is used here to facilitate comparison.

A. Structure factor

In contrast to previous work, here we will compare experiment with theory on an absolute scale. We therefore begin by presenting relations between the scattering cross section, the structure factor, and the composition variable. The spatial composition distribution in a system at a given time can be characterized by the single-time, two-point correlation function

$$S(\mathbf{r},t)\equiv\frac{1}{V}\int_V \Delta c(\mathbf{r}',t)\Delta c(\mathbf{r}'+\mathbf{r},t)d\mathbf{r}' , \tag{2}$$

where V is the volume of the system and $\Delta c(\mathbf{r},t)\equiv c(\mathbf{r},t)-c_0$ is the composition deviation from its average value c_0 as a function of position $\mathbf{r}$ and time t. The correlation function is time dependent because the system is not at equilibrium. The structure factor is the Fourier transform of the correlation function, given by

$$\hat{S}(\mathbf{k},t)\equiv\int_\infty S(\mathbf{r},t)\exp(i\mathbf{k}\cdot\mathbf{r})d\mathbf{r} . \tag{3}$$

It is convenient to associate the structure factor with the strength of the composition waves in the system, since it is equal to the intensity (the square of the amplitude) of the Fourier transform of the composition distribution. In the present case, the system is isotropic, and so the correlation function and structure factor depend only on the magnitudes r and k of the position and wave vectors $\mathbf{r}$ and $\mathbf{k}$, respectively. They also depend on the units chosen for the composition variable.

The structure factor can be obtained directly from x-ray-scattering measurements, since it is simply proportional to the scattering cross section per unit volume:[37]

$$\hat{S}(k,t)=r_e^{-2}\left[\frac{d\rho^e}{dc}\right]^{-2}\frac{d\sigma_V}{d\Omega}(2\theta,t) . \tag{4}$$

Here $r_e=2.82\times10^{-13}$ cm is the classical electron radius, and the derivative $d\rho^e/dc$ is the proportionality between electron density and the composition variable. The scattering angle 2θ and wave number k are related by $k=4\pi\sin\theta/\lambda$. These equations have been used to convert the measured cross sections to structure factors. The composition variable chosen for this analysis is the total mole fraction of the modifier c of expression (1). The value of the coefficient $d\rho^e/dc$ was estimated from measurements of the mass density. The electron density ρ^e, mass density ρ^m, and molecular density ρ are related by

$$\rho^e(c)=[ce_1+(1-c)e_2]\rho(c) , \tag{5a}$$

$$\rho^m(c)=[cm_1+(1-c)m_2]\rho(c) , \tag{5b}$$

where e_1 and e_2 (m_1 and m_2) are the number of electrons (the mass) of the modifier and network components, respectively, given in expression (1). The measured mass densities of samples of composition $c=0.10$ and 0.12 are given in Table I, along with calculated molecular and electron densities. A value of $d\rho^e/dc=6.43\pm0.44\times10^{23}$ cm^{-3} was obtained from these room-temperature densities. (An estimate of the composition dependence of the expansion coefficient indicates that the high-temperature value may be $\sim 7\%$ smaller.)

TABLE I. Measured mass densities and calculated molecular and electron densities for samples of two compositions at room temperature. The composition variable c and the molecular density ρ are based on the molecular units of expression (1).

c	ρ^m (g cm^{-3})	ρ (10^{22} cm^{-3})	ρ^e (10^{23} cm^{-3})
0.10	2.458±0.001	2.228±0.001	7.240±0.003
0.12	2.511±0.002	2.233±0.002	7.369±0.006

B. Cahn-Hilliard-Cook theory

Classical theories for the evolution of the structure factor during spinodal decomposition are based on the solution of a diffusion equation which includes the effect of a "gradient energy" term in the free-energy functional of a system of nonuniform composition.[38] The free-energy functional F is expressed as the integral over the system of a free-energy-density expansion containing terms representing bulk, gradient, and elastic energy contributions. Introducing the gradient energy term into the expression used in Ref. 28, one obtains

$$F=\int_V(\rho f+\rho\kappa|\nabla c|^2+\tfrac{1}{2}\sigma:\epsilon_{\rm el})d\mathbf{r}\ . \tag{6}$$

Here f is the free energy per molecule of an unstressed system of uniform composition, κ is a coefficient giving the contribution from composition gradients, and the last term is the elastic-energy density. The thermodynamic "driving force" used in the diffusion equation is obtained by taking a variational derivative of the free-energy functional.

The simplest solution for the structure factor is obtained[1] by neglecting all nonlinear terms in the diffusion equation, under the assumption that composition deviations are sufficiently small. When the elastic-energy term is neglected and equilibrium fluctuations are properly taken into account,[23,24,39] one obtains

$$\frac{\partial\hat{S}(k,t)}{\partial t}=2R(k)[\hat{S}(k,t)-\hat{S}_{\rm OZ}(k)]\ , \tag{7}$$

where $\hat{S}_{\rm OZ}(k)$ is the Ornstein-Zernike form[40] for the equilibrium structure factor at temperature T,

$$\hat{S}_{\rm OZ}(k)\equiv\frac{k_BT}{\rho_0(f''+2\kappa_0k^2)}\ , \tag{8}$$

and $R(k)$ is the "amplification factor," given by

$$R(k)=-[(1-c_0)M_{10}+c_0M_{20}]k^2c_0(1-c_0)\times(f''+2\kappa_0k^2)\ . \tag{9}$$

Here k_B is the Boltzmann constant, f'' is defined by

$$f''\equiv\left.\frac{d^2f}{dc^2}\right|_{c=c_0}\ , \tag{10}$$

and M_1 and M_2 are the mobilities of the modifier and network species, respectively. The subscript zeroes on ρ, κ, M_1, and M_2 indicate evaluation at the average composition c_0. (In the present study, $c_0=0.10$.) The coefficient κ_0 is positive at all temperatures; f'' is positive at high temperatures, but is negative at low temperatures where the single-phase state is thermodynamically unstable.

The definition of f as free energy per molecule rather than as free energy per unit volume is necessary in systems where the molecular density ρ is composition dependent, because the coefficient f'' appearing in results such as Eqs. (8) and (9) should not depend on $d\rho/dc$ or $d^2\rho/dc^2$. Although this distinction was understood in early work,[1] the definition of f as free energy per unit volume has often appeared in subsequent work,[9,23,24,39] including the original article on DIF theory.[26] This point is especially important in the analysis of data from an amorphous oxide system, where many choices of composition variable are plausible.

When the temperature and the material parameters (and hence $\hat{S}_{\rm OZ}$ and R) are constant in time, the solution to the linear differential equation (7) for the structure factor can be expressed as

$$\Delta\hat{S}(k,t)=[\hat{S}_{\rm OZ}(k)-\hat{S}(k,0)]\{1-\exp[2R(k)t]\}\ , \tag{11}$$

where $\hat{S}(k,0)$ is the structure factor of the reference state at $t=0$, and $\Delta\hat{S}(k,t)$ is the structure factor change relative to this reference state:

$$\Delta\hat{S}(k,t)\equiv\hat{S}(k,t)-\hat{S}(k,0)\ . \tag{12}$$

It is convenient to use Eq. (11) for comparison with the data because the structure factor change $\Delta\hat{S}(k,t)$ is the quantity measured most accurately in the phase-separation runs, as discussed above.

For the present study, we wish to consider the CHC predictions for a system initially prepared in a single-phase equilibrium state at temperature T_1, which is quenched at time $t=0$ to a final temperature T_2. If T_2 is outside of the unstable region, f'' is positive, the amplification factor R is negative for all k, and the structure factor reequilibrates at long times for all k to the equilibrium structure factor $\hat{S}_{\rm OZ}(k)$ evaluated at the final temperature T_2. This reequilibration of the structure factor occurs by a simple exponential relaxation at each wave number. The wave-number dependence of the relaxation rate is given by $R(k)$. Alternatively, if T_2 is within the unstable region, where f'' is negative, the amplification factor is positive for k lower than a critical wave number k_c, given by

$$k_c\equiv\left[\frac{-f''}{2\kappa_0}\right]^{1/2}\ . \tag{13}$$

At wave numbers lower than k_c, the structure factor increases exponentially without bound, corresponding to the growth of the two-phase structure. At wave numbers higher than k_c, the amplification factor is negative, and $\hat{S}$ reequilibrates to $\hat{S}_{\rm OZ}$ evaluated at T_2 just as for a quench to a temperature outside of the unstable region. At the critical wave number k_c, the structure factor grows linearly with time.

C. Fit of CHC theory to data

To calculate the structure factor change $\Delta\hat{S}(k,t)$, the reference structure factor $\hat{S}(k,0)$ is needed on the right-hand side of Eq. (11). The time $t=0$ is taken to be the time of the quench, and so $\hat{S}(k,0)$ is the equilibrium structure factor at $T_1=1074$ K. The reference structure factor $\hat{S}(k,0)$ used to analyze all of the phase-separation data is taken to be the best fit of the Ornstein-Zernike form of Eq. (8) to the measured structure factor at T_1 obtained from run Z. Table II shows the values of $\rho_0 f''$ and $\rho_0\kappa_0$ derived from this fit, along with the reduced chi-square value χ_ν^2 and the multiple correlation coefficient.[41] As in all fit results presented in this work, these goodness-of-fit parameters are calculated using the known variance in each data point due to photon-counting statistics and electronic noise. The uncertainties in the derived parameter values are listed as ± one standard deviation.

At all final temperatures T_2 studied, the general behavior of the structure factor measured during phase separation is described qualitatively by the CHC theory. This correspondence can be seen in the typical data from run A, shown in Fig. 5. The structure factor approaches a constant asymptote at high wave numbers, while continuing to grow at low wave numbers. Furthermore, the high-wave-number asymptote is well described by $\hat{S}_{OZ}$ defined in Eq. (8). This is shown in Fig. 9, where structure factors measured at several temperatures have been plotted as $k_B T/\hat{S}$ vs k^2. A straight line on such a plot is indicative of the Ornstein-Zernike form. The set of experimental points for $T=1074$ K is from run Z, and the line through them is the fit described above used for $\hat{S}(k,0)$. Each set of points shown for one of the lower temperatures is obtained by adding this $\hat{S}(k,0)$ to the structure factor change $\Delta\hat{S}(k,t)$ measured late in a phase-separation run. The points for $T=1014$ K are from run E at 1413 sec after the quench, and the points for $T=969$ K are from run C at 2642 sec after the quench. Lines through these data sets are Ornstein-Zernike asymptotes obtained from fits described in Sec. III F below. The intercept at $k=0$ gives the value of $\rho_0 f''$ for that temperature. This quantity is positive at higher temperatures and negative at lower temperatures, consistent with the thermodynamic description used in the CHC theory.

Although the linearized thermodynamics of the CHC theory describes the data well, the kinetics of the model does not. Figure 10 shows the best fit of the CHC theory to the data of run A. This fit was obtained using expressions (8) and (9) in the solution (11), allowing the three

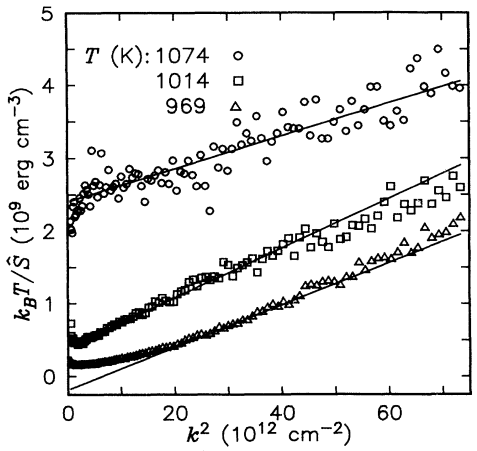

FIG. 9. Ornstein-Zernike plot of structure factors from several temperatures, showing Lorentzian shape of high-wave-number tail. Solid lines are asymptotes from DIF-theory fits (see text).

parameters $\rho_0 f''$, $\rho_0\kappa_0$, and $[(1-c_0)M_{10}+c_0 M_{20}]/\rho_0$ to vary. (Although data and theory from only a selection of times is shown in the figure, the fit is typical of all such fits in this work in that it involves all experimental points obtained in the run, in this case 24 times at each of 100 wave numbers.) One can see that the fit is very poor; it has a reduced chi-square value of $\chi_\nu^2 \simeq 52$ and a correlation coefficient of ~ 0.90. Likewise, the fits of the CHC theory to the data of every run are very poor, with the discrepancy between theory and experiment increasing at lower temperatures. The nature of the discrepancy is the same at all temperatures: The theory predicts that $\hat{S}$ should relax to the asymptote $\hat{S}_{OZ}$ much more rapidly at high wave numbers than at low wave numbers, while such a strong wave-number dependence of the relaxation rate is not exhibited by the data. Thus the peak in the experimental data always occurs at a lower wave number than the peak in CHC theory when the high-wave-number asymptotes agree. Detailed support for this interpretation can be seen in the time dependence of the experimental and theoretical structure factor changes at two wave numbers shown in Fig. 11. At the higher wave number, both the measured $\Delta\hat{S}$ and CHC solution relax exponentially, while at a wave number near the critical wave number estimated from the asymptote ($k_c \simeq 1\times 10^6$ cm^{-1}) both grow almost linearly in time. Thus the measured data agree well with the thermodynamics of the

TABLE II. Values of the two parameters obtained from the best fit of the Ornstein-Zernike form (8) to the equilibrium structure factor at $T_1=1074$ K from run Z. Also given are the reduced chi square χ_ν^2 and the multiple correlation coefficient R^2 for the fit.

Run	T (K)	$\rho_0 f''$ (10^8 erg cm^{-3})	$\rho_0\kappa_0$ (10^{-5} erg cm^{-1})	χ_ν^2	R^2
Z	1074	24.0±0.5	1.12±0.05	1.5	0.80

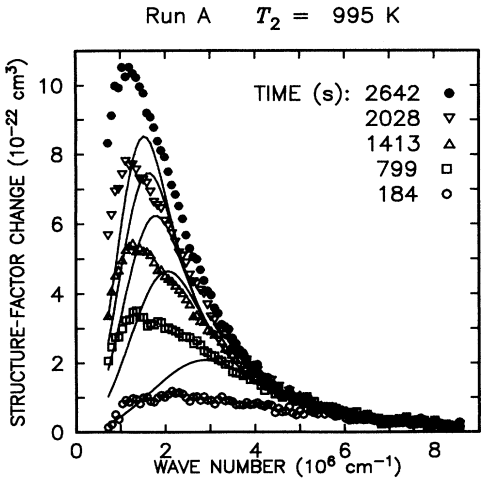

FIG. 10. Structure factor change as a function of wave number at several times measured in run A (symbols), compared with the best fit obtained using the CHC theory (solid lines).

CHC theory, which gives factors of $(1-k^2/k_c^2)^{-1}$ in both $\hat{S}_{OZ}$ and R^{-1}. However, the CHC kinetic factor proportional to k^2 in R does not describe the data well, since the wave-number dependence of the slopes of the theory and the data do not match in Fig. 11.

D. Diffusion induced flow theory

During initial attempts to fit the data,[25] we observed that the shapes of the measured structure factors as a function of wave number are described much more closely by the theory if the first k^2 factor in the amplification factor of Eq. (9) is not included. This factor arises from

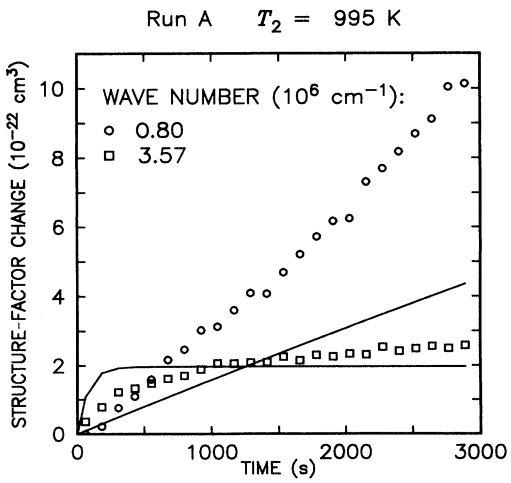

FIG. 11. Structure factor change as a function of time at two wave numbers measured in run A (symbols), compared with the best fit obtained using the CHC theory (solid lines).

the Laplacian in the basic diffusion equation used to model the kinetics. An equation which does not contain the Laplacian is characteristic of a relaxation process, rather than a diffusion process. This observation led directly to the consideration of stress generation and relaxation during interdiffusion in amorphous systems, and the development of diffusion-induced-flow (DIF) theory.

A linearized spinodal decomposition theory incorporating these effects was presented in a previous article.[26] This work was essentially an extension of the original treatment of coherency stress during spinodal decomposition[1] to include the effects of stress relaxation. This treatment was subsequently recast for the general case of interdiffusion.[27,28] In this DIF theory, one considers both the generation of stress owing to unequal mobilities of the diffusing species and the relaxation of this stress through deformation. For a typical glass-forming oxide system, in which the mobility of the network modifier species is much larger than the mobility of the network former, the DIF theory predicts that the rate-limiting step for interdiffusion of modifier and network species can change between viscous flow of the network and diffusion of the modifier depending on the length scale of the composition gradient.

Here the notation developed for the general case[28] will be used to express the original results for spinodal decomposition.[26] This linearized DIF theory yields the same differential equation for the structure factor as the CHC theory [Eq. (7)] with the same expression for $\hat{S}_{OZ}$ [Eq. (8)], but with a modified expression for the amplification factor:

$$R(k)=-\frac{3(1-c_0)^2}{4\rho_0^2\bar{V}_{10}^2\eta_0}\frac{k^2}{k^2+k_e^2}\rho_0(f''+2\kappa_0 k^2)\ . \tag{14}$$

Here η is the viscosity, $\bar{V}_1$ is the partial molal volume of the modifier species, and k_e is the "exchange wave number," defined by

$$k_e^2\equiv\frac{3}{4c_0M_{10}\rho_0\bar{V}_{10}^2\eta_0}\ . \tag{15}$$

Once again, the subscript zeros on η and $\bar{V}_1$ indicate evaluation at c_0. This expression for the amplification factor is valid for wave numbers smaller than a characteristic wave number k_d,

$$k^2\ll k_d^2\equiv\frac{3\rho_0(1-c_0)}{4\eta_0M_{20}}\ , \tag{16}$$

and for times larger than a quasi-steady-state induction time t_{QSS},

$$t\gg t_{QSS}\equiv\frac{6\eta_0}{Y}\frac{k_e^2}{k^2+k_e^2}\ , \tag{17}$$

where Y is an elastic modulus.[28] It is derived for the limiting case in which the mobility of the modifier species is much larger than the mobility of the network former, so that the ratio q_m between k_e and k_d is negligible with respect to unity:

$$1 \gg q_m^2 \equiv \frac{k_e^2}{k_d^2} = \frac{1}{c_0(1-c_0)\rho_0^2 \bar{V}_{10}^2} \left[\frac{M_{20}}{M_{10}} \right] . \quad (18)$$

It is also derived for the limit in which the chemical energy coefficient is negligible with respect to the elastic-energy coefficient:

$$|\rho_0 f''| \ll \frac{2Y\rho_0^2 \bar{V}_{10}^2}{9(1-c_0)^2} . \quad (19)$$

The expression (14) for the amplification factor is used here under the assumption that conditions (16)–(19) are satisfied. In particular, it is assumed that k_d is much larger than the wave-number range of interest and that t_{QSS} is negligible with respect to the time scale of the experiment. The validity of these assumptions is considered in Sec. IV.

Using the composition basis given in expression (1), the two molecular species considered are the average network modifier ($\frac{1}{2}BaO \cdot \frac{1}{2}K_2O$) and the network former (SiO_2). The DIF mechanism for spinodal decomposition can be envisioned as clustering of modifier via diffusion coupled with nonuniform dilation of the network involving viscous flow. The rate-limiting step changes as a function of wave number: For $k > k_e$, viscous flow of the

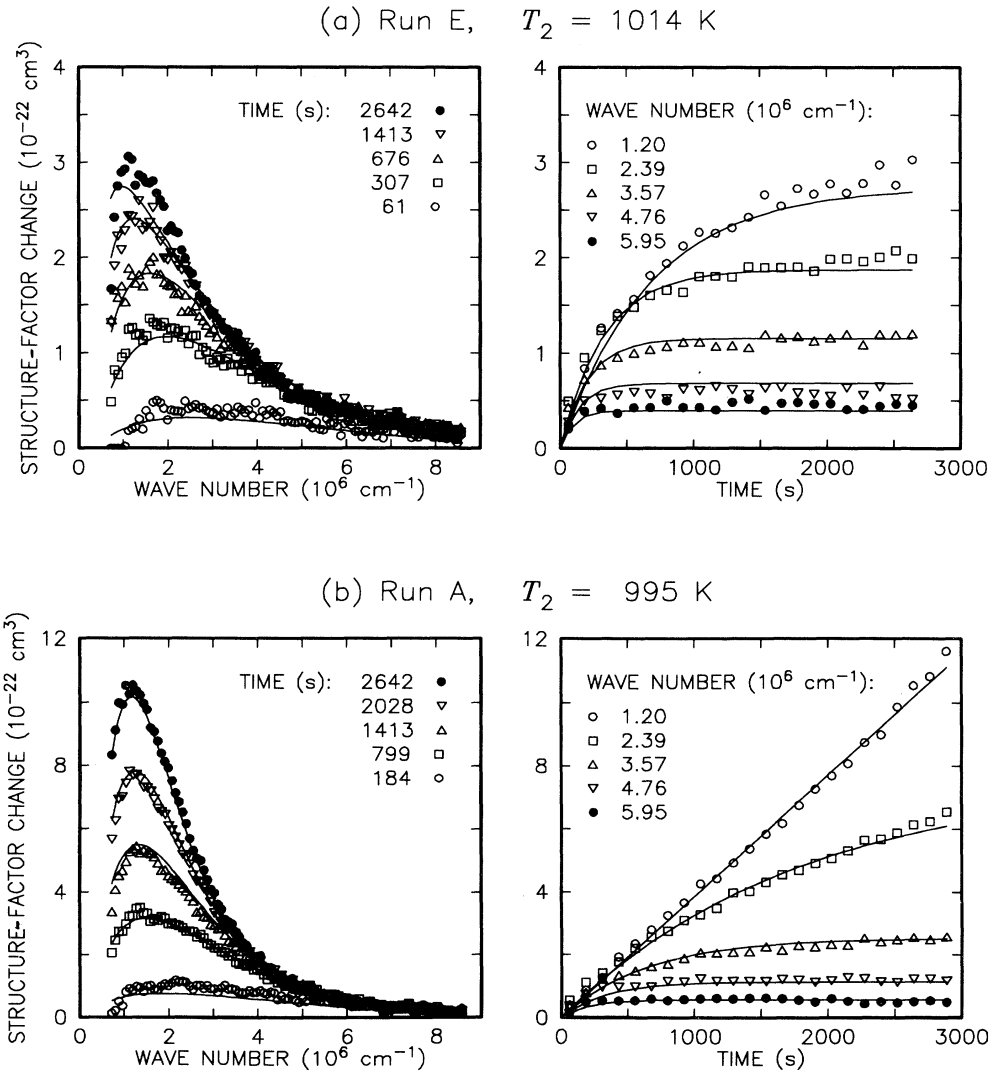

FIG. 12. Fit of DIF theory (solid lines) to experimental data (symbols) from runs at each temperature. Each fit is over the complete data set recorded. Structure factor change is plotted both as a function of wave number at several times and as a function of time at several wave numbers for each run.

network is rate limiting; for $k < k_e$, diffusion of modifier is rate limiting. If the viscosity is relatively small, k_e is large, and the DIF result (14) for the amplification factor reduces to the standard CHC result (9). Conversely, if the viscosity is relatively large, k_e is small, and the DIF amplification factor does not have the k^2 dependence characteristic of a diffusion process.

E. Fit of DIF theory to complete runs

The DIF spinodal decomposition theory is compared with scattering data from runs at all four temperatures in Fig. 12. Since the data from pairs of runs with the same final temperature T_2 (i.e., runs A and B, C and F) were quite reproducible, only one of each pair is shown. For each run, two graphs are presented: the change in the structure factor as a function of wave number at several fixed times and the change in the structure factor as a function of time at several fixed wave numbers. The theory curves shown for each run are from the best fit obtained using the DIF expressions (8) and (14) in solution (11), allowing the four parameters $\rho_0 f''$, $\rho_0 \kappa_0$, $\rho_0^2 \bar{V}_{10}^2 \eta_0$, and k_e to vary. Parameter values obtained from fits to all six runs are summarized in Table III.

For all times and temperatures, good agreement is obtained using the DIF theory. The shapes of the structure factor as a function of wave number given by the DIF theory agree much better with the experimental data than the shapes given by the CHC theory. This is reflected in the goodness-of-fit parameter values: The χ_ν^2 improve to ~ 3 from ~ 50, and the correlation coefficients improve to ~ 0.99 from ~ 0.90. The better agreement of DIF theory is also shown by the k_e values obtained. If k_e were larger than the wave-number range

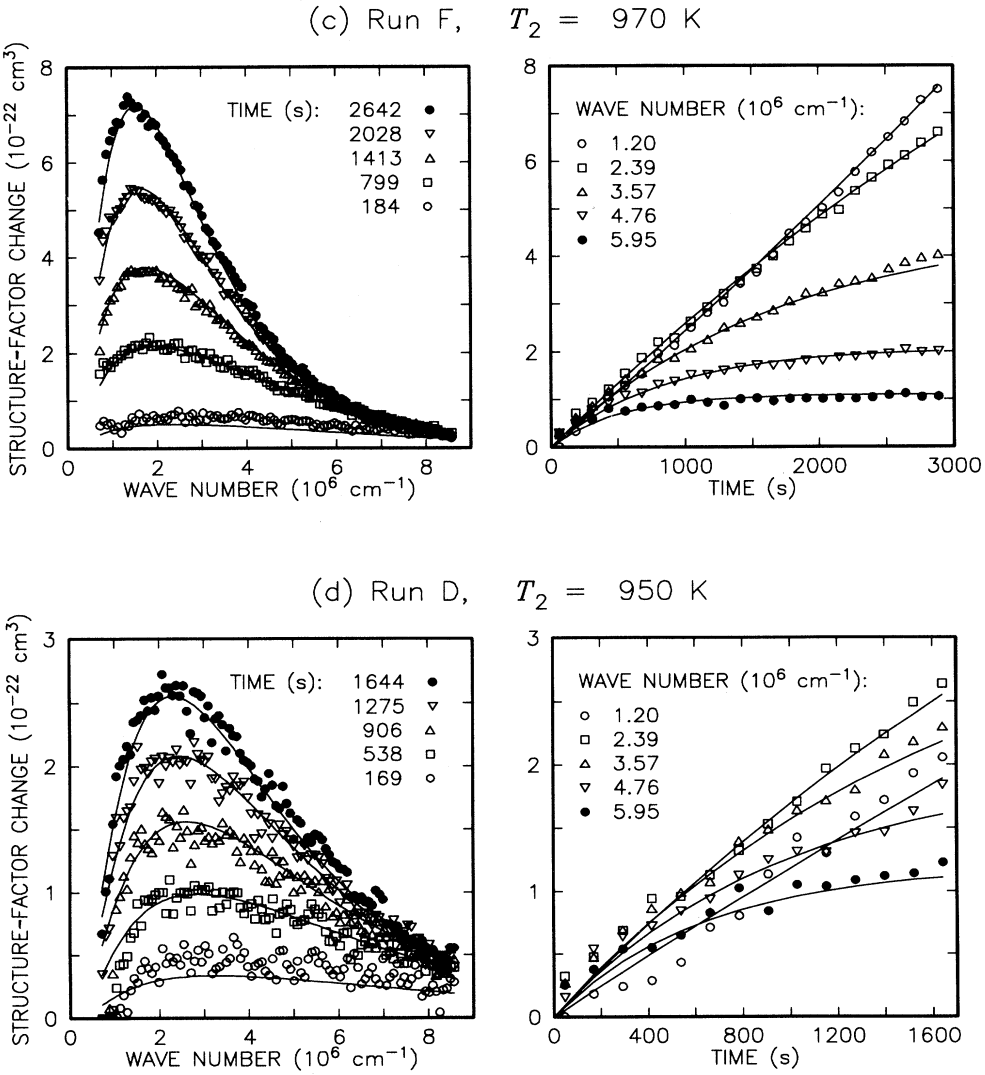

FIG. 12. (*Continued*).

TABLE III. Values of the four parameters obtained from the best fit of the DIF theory to the complete data set from each run. Also given are the reduced chi square χ_ν^2 and the multiple correlation coefficient R^2 for each fit.

Run	T (K)	$\rho_0 f''$ (10^8 erg cm^{-3})	$\rho_0\kappa_0$ (10^{-5} erg cm^{-1})	$\rho_0^2\bar{V}_{10}^2\eta_0$ (10^{11} P)	k_e (10^5 cm^{-1})	χ_ν^2	R^2
E	1014	3.66±0.02	1.78±0.01	1.87±0.04	10.8±0.3	2.0	0.9804
A	995	−0.55±0.01	1.95±0.01	3.40±0.02	6.2±0.1	2.7	0.9948
B	995	−0.43±0.01	1.89±0.01	3.51±0.02	5.6±0.1	2.3	0.9943
C	969	−0.77±0.02	1.31±0.01	4.94±0.03	7.0±0.1	3.3	0.9942
F	970	−0.80±0.02	1.31±0.01	5.16±0.03	7.2±0.1	3.0	0.9951
D	950	0.63±0.08	1.02±0.01	5.88±0.08	12.5±0.2	1.6	0.9697

of interest, then the DIF and CHC theories would be almost equivalent. However, the best-fit values of k_e are found to be small. This indicates that viscous flow of the network is the rate-limiting step for interdiffusion over virtually all of the wave-number range observed, which corresponds to composition deviation wavelengths up to ~1000 Å. The agreement between spinodal decomposition theory and experiment shown in Fig. 12 is by far the best and most extensive yet found in studies of amorphous oxide systems.

The overall fits of the DIF theory are sufficiently good that one can identify regions in which there are small systematic deviations between the theory and experimental data. The main systematic deviation occurs at the beginning of each run. In every case, over almost the complete wave-number range observed, the measured structure factor initially increases more rapidly than the best fit to the complete run. Such initial behavior could be attributed to the establishment of the quasi-steady-state condition (17). Alternatively, such behavior would occur if the material parameters were not constant in time after the quench, because of an additional process such as structural relaxation of the glass. A second systematic deviation also occurs in the fits to the runs at the higher final temperatures, *E* and *A*. At the lowest wave numbers, the measurement increases above the theory at late times. The low-wave-number, late-time deviation is most prominent in run *E*, which is predicted to be at a temperature outside the unstable region. Such behavior might be expected if nucleated phase separation were to occur, since nucleation is not modeled by the spinodal decomposition theory.

F. Fit to DIF theory to truncated runs

In order to investigate the small deviations between theory and data shown in Fig. 12, fits were made over time intervals shorter than complete runs. This was possible because the initial condition for solving the linear differential equation (7) is arbitrary and can be taken to be the measured structure factor at any time $t=t_i$ during a run. The solution for the structure factor change [relative to the same reference state $\hat{S}(k,0)$ as above] is then given by

$$\Delta\hat{S}(k,t)=\Delta\hat{S}(k,t_i)+[\hat{S}_{OZ}(k)-\hat{S}(k,0)-\Delta\hat{S}(k,t_i)]\times\{1-\exp[2R(k)(t-t_i)]\}\ , \tag{20}$$

where $\Delta\hat{S}(k,t_i)$ is the structure factor change which gives the initial condition at $t=t_i$. A smooth curve (cubic spline) fit through the measured structure factor change for time t_i after the quench was used as $\Delta\hat{S}(k,t_i)$.

The apparent changes in the material parameter values with time during a run were studied by separately fitting every set of four consecutive scattering patterns using the DIF expressions (8) and (14) in solution (20), allowing $\rho_0 f''$, $\rho_0\kappa_0$, $\rho_0^2\bar{V}_{10}^2\eta_0$, and k_e to vary. Best-fit parameter values obtained from such "running fits" to a typical run (*B*) are plotted as a function of time in Fig. 13. Each bar shows the time interval corresponding to the set of scattering patterns involved in that fit. The parameters evolve in a systematic rather than random manner, indicating that all four parameters are reasonably well determined even by these short intervals of data. In all runs the values of $\rho_0 f''$, $\rho_0\kappa_0$, and $\rho_0^2\bar{V}_{10}^2\eta_0$ change relatively rapidly at first and then progressively more slowly. The direction of this change is always from a high-temperature value toward a low-temperature value, and the size of the change is larger for quenches to lower temperatures. Values of k_e always remain small relative to the wave-number range of the data, indicating that the DIF theory fits the data better than the CHC theory even when the parameters are allowed to vary with time.

To minimize possible effects of structural relaxation and nucleation, fits were made to truncated data sets from each run in which the first few patterns after the quench (and the last few patterns in runs *A*, *B*, and *E*) were not included. Table IV summarizes the parameter values obtained from these fits, using the DIF expressions (8) and (14) in solution (20), allowing the three parameters $\rho_0 f''$, $\rho_0\kappa_0$, and $\rho_0^2\bar{V}_{10}^2\eta_0$ to vary. The value of k_e was fixed for all runs at the average value found in the running fits, $k_e=5.2\times10^5$ cm^{-1}. The values of χ_ν^2 obtained from these fits indicate that the DIF theory describes this major portion of the data with little significant deviation.

The temperature dependence of the values of $\rho_0 f''$, $\rho_0\kappa_0$, and $\rho_0^2\bar{V}_{10}^2\eta_0$ obtained from the fits of DIF theory are shown in Figs. 14, 15, and 16, respectively. Parame-

TABLE IV. Values of the three parameters obtained from the best fit of the DIF theory to a truncated data set from each run. Also given are the reduced chi square χ_ν^2 and the multiple correlation coefficient R^2 for each fit.

Run	T (K)	t_i (sec)	$\rho_0 f''$ (10^8 erg cm^{-3})	$\rho_0\kappa_0$ (10^{-5} erg cm^{-1})	$\rho_0^2\bar{V}_{10}^2\eta_0$ (10^{11} P)	χ_ν^2	R^2
E	1014	307	3.95±0.04	1.71±0.01	2.78±0.12	1.4	0.9838
A	995	430	−0.43±0.03	1.93±0.01	3.83±0.04	1.3	0.9965
B	995	430	−0.44±0.04	1.90±0.01	4.00±0.05	1.3	0.9957
C	969	553	−1.86±0.03	1.45±0.01	7.22±0.06	1.6	0.9976
F	970	553	−1.78±0.03	1.45±0.01	7.40±0.06	1.5	0.9977
D	950	538	−2.87±0.15	1.23±0.01	12.92±0.25	1.2	0.9757

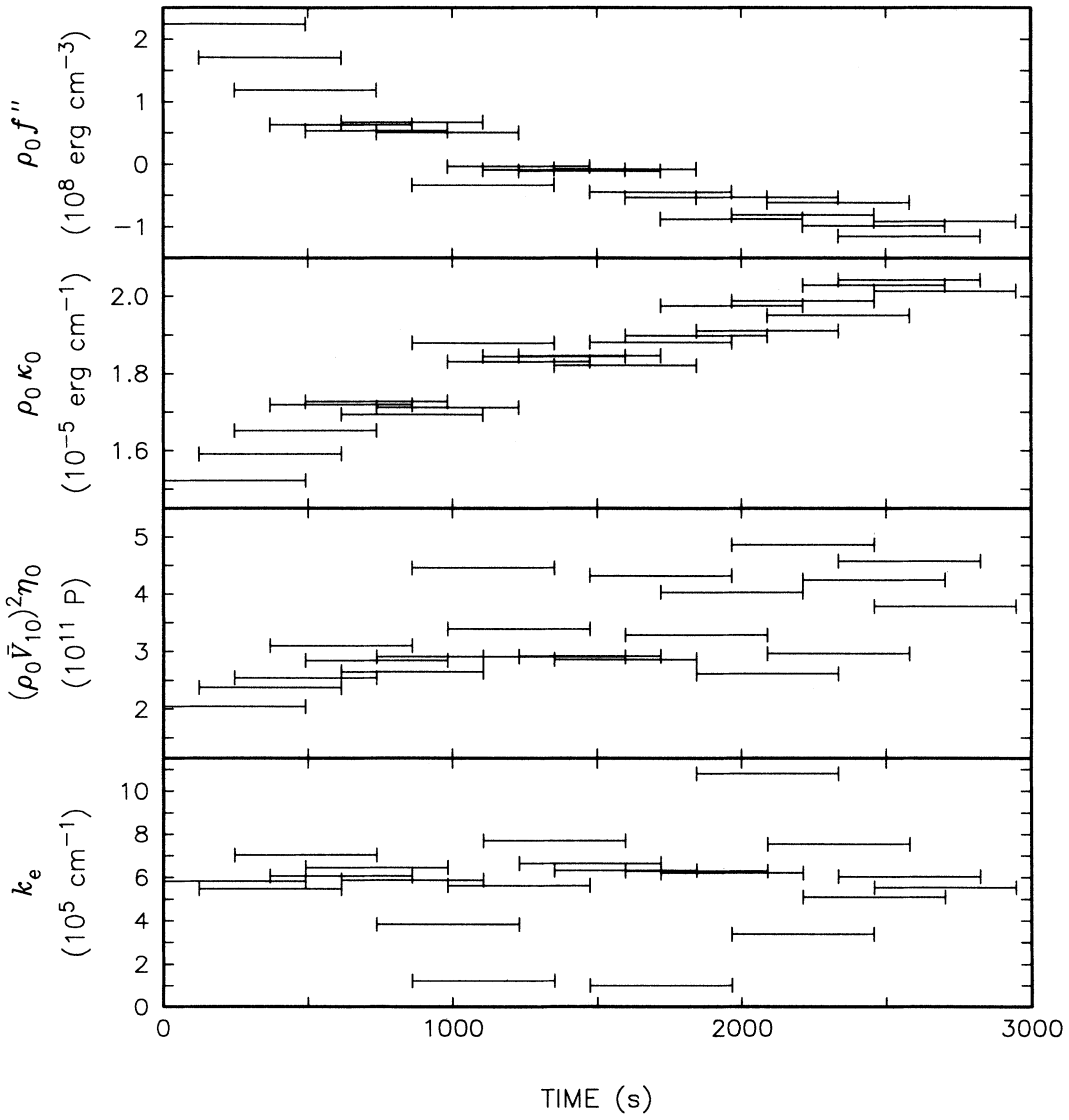

FIG. 13. Parameter values as a function of time from running fits to every four consecutive scattering patterns from run *B*, $T_2 = 995$ K.

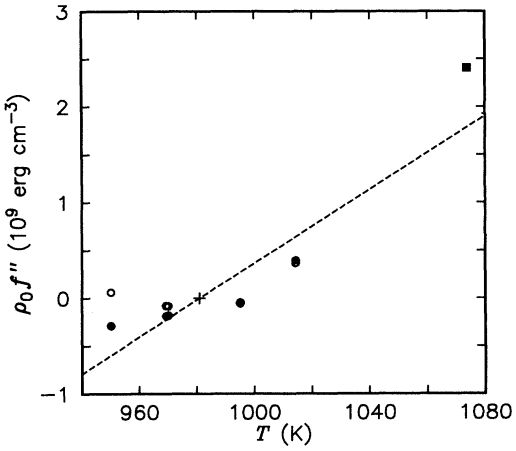

FIG. 14. Values of $\rho_0 f''$ as a function of temperature. Open circles: values from DIF-theory fits to complete runs $A-F$. Solid circles: values from DIF-theory fits to truncated runs $A-F$. Square: value from Ornstein-Zernike fit to run Z. Dashed line: regular solution estimate; cross marks mean-field spinodal.

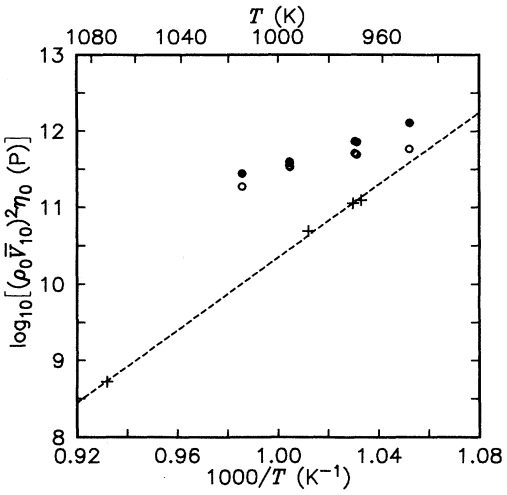

FIG. 16. Values of $\log_{10}[\rho_0^2 \bar{V}_{10}^2 \eta_0$ (D)] as a function of inverse temperature. Open circles: values from DIF-theory fits to complete runs $A-F$. Solid circles: values from DIF-theory fits to truncated runs $A-F$. Crosses and dashed line: estimates from viscosity measurements.

ter values from fits to complete runs and fits to truncated runs are shown with open and solid symbols, respectively. (The dashed lines in Figs. 14 and 16 are independent estimates discussed in Sec. IV A below.) The fits to the truncated runs give parameter values which have somewhat more reasonable temperature dependences. In particular, the truncation yields the expected negative value of $\rho_0 f''$ for the lowest temperature. The differences between the values obtained from the two types of fits are larger at the lower temperatures (runs C, D, and F), where the systematic deviations at the beginning of the runs are larger in the fits to the complete runs. For these deeper quenches, the structural relaxation time is expected to be a larger fraction of the time period of the measurement, and the amplitude of the structural relaxation is expected to be greater. The values of $\rho_0 f''$ and $\rho_0 \kappa_0$ from the fits to truncated runs E and C were used for the calculated Ornstein-Zernike asymptotes shown in Fig. 9 above.

Because of inaccuracy in absolute detector calibration and in the estimation of $d\rho^e/dc$, the overall scale for all structure factors reported above may be in error by as much as a factor of 1.6. Such error would change all derived values of $\rho_0 f''$, $\rho_0 \kappa_0$, and $\rho_0^2 \bar{V}_{10}^2 \eta_0$ by the same factor, although it would not affect ratios such as k_c and k_e. This uncertainty is not reflected in the standard deviations listed in Tables II–IV.

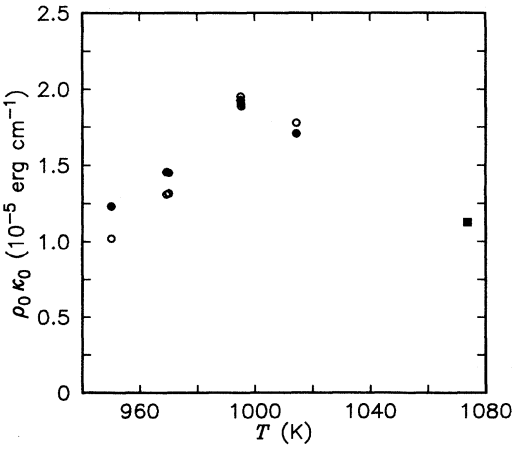

FIG. 15. Values of $\rho_0 \kappa_0$ as a function of temperature. Open circles: values from DIF-theory fits to complete runs $A-F$. Solid circles: values from DIF-theory fits to truncated runs $A-F$. Square: value from Ornstein-Zernike fit to run Z.

IV. DISCUSSION

The material properties entering into spinodal decomposition theory such as $\rho_0 f''$, $\rho_0 \kappa_0$, and $\rho_0^2 \bar{V}_{10}^2 \eta_0$ have been treated as free parameters when fitting the theory to the scattering data. Even when arbitrary values were allowed, it was not possible to obtain any reasonable fits with the CHC theory. On the other hand, good fits to all of the data were obtained using the DIF theory. The good agreement allowed us to make a direct comparison between experimental and theoretical structure factors as a function of wave number and time, rather than the less definitive comparison of amplification factors, which has been used in all previous analyses.[4–7,11,17] By directly comparing structure factors on an absolute scale, we were able to obtain separate values for each thermodynamic and kinetic parameter, rather than only combinations such as the effective interdiffusion coefficient and the critical wave number. In the next section we evaluate the DIF theory fits by comparing the parameter values ob-

tained to independent estimates. We also verify that all four of the self-consistency conditions (16)–(19) are satisfied.

A. Comparison of fit parameter values with independent estimates

The values of $\rho_0 f''$ obtained from the fits can be compared to those calculated from the regular-solution fit to the phase diagram, presented in the Appendix. The regular-solution result for $\rho_0 f''$ as a function of temperature is shown as a dashed line in Fig. 14. The mean-field spinodal temperature from the regular solution model, $T_s = 981$ K, is shown as a cross. This value is significantly lower than the observed instability point, as determined by the change in sign of the values of $\rho_0 f''$ given in Table IV, which occurs at $T_s \simeq 998$ K. This may be an indication of the finite range of the molecular interactions in this system. When interactions are of finite range, the observed instability point is expected to lie between the mean-field estimate and the two-phase coexistence boundary.[20] The regular-solution result (A11) relates the temperature derivative of $\rho_0 f''$ to the density of the molecules used to calculate the configurational entropy. A value of $N = 1$ for the size of the molecular units in expression (A1) was used to give the dashed line in Fig. 14. The good agreement with the values of $\rho_0 f''$ obtained from the fits indicates that their magnitude is physically reasonable.

For self-consistency, the values of $\rho_0 f''$ obtained from the DIF theory fits must satisfy condition (19) relating the chemical and elastic-energy coefficients. A value for the partial molal volume of the modifier is needed for this and other comparisons below. The partial molal volume is related to the composition dependence of the molecular density by

$$\rho_0 \overline{V}_{10} = 1 - \frac{1-c_0}{\rho_0} \left. \frac{d\rho}{dc} \right|_{c=c_0} . \tag{21}$$

From the room-temperature values in Table I, one obtains $\rho_0 \overline{V}_{10} = 0.89 \pm 0.06$. (The high-temperature value may be ~7% larger.) Using a typical value for the elastic modulus $Y \simeq 5 \times 10^{11}$ erg cm^{-3}, the right-hand side of the inequality (19) can be evaluated as $\sim 1 \times 10^{11}$ erg cm^{-3}. This is much larger in magnitude than any of the values of $\rho_0 f''$ obtained from the fits, and so the condition (19) is satisfied. From the observed temperature derivative of $\rho_0 f''$, one can estimate the suppression of the "coherent spinodal,"[1,26] i.e., the lowering of the instability temperature which would occur if stress relaxation were not possible. At the coherent spinodal temperature, relation (19) would be an equality. Extrapolating $\rho_0 f''$ to lower temperatures using the measured value $\rho_0 f'' = -2.87 \times 10^8$ erg cm^{-3} at $T - T_s = -48$ K, one finds that the instability temperature would be lowered by ~18 000 K, an unphysically large amount. One therefore expects that the coherent instability is completely suppressed and that stress relaxation is necessary for spinodal decomposition at all temperatures.

To estimate values of $\rho_0^2 \overline{V}_{10}^2 \eta_0$ for comparison with those obtained from the fits, the viscosity of samples of composition $c = 0.10$ was measured at four temperatures between 950 and 1100 K using a parallel-plate viscometer. The samples were initially single phase. The early stage of phase separation did not affect the macroscopic viscosity, since it remained constant during the first hour at temperatures in the two-phase region. (Time dependence of the viscosity after an abrupt quench, as shown in Fig. 13, could not be verified because of the slow temperature response of the viscometer.) The measured viscosities are well described by the Arrhenius form $\eta_0 = (5.3 \times 10^{-14}\ \text{P}) \exp[(4.71\ \text{eV})/k_B T]$. Values of $\rho_0^2 \overline{V}_{10}^2 \eta_0$ obtained from the viscosity measurements are shown as crosses and a dashed line in Fig. 16. The fit values agree with these absolute estimates within about one order of magnitude.

The quasi-steady-state induction time t_{QSS} of condition (17) can be estimated from the fit values of $\rho_0^2 \overline{V}_{10}^2 \eta_0$ given in Table IV. Using the values of Y and $\rho_0 \overline{V}_{10}$ given above, one obtains maximum values of t_{QSS} at $k = 0$ ranging between 4 and 20 secs. Since this is much smaller than the time resolution of the experiment, condition (17) is self-consistent. To check condition (16), one can assume that η_0 and M_{20} are related by a Stokes-Einstein expression[28]

$$\eta_0 = \frac{\rho_0 d_{\text{SE}}^2}{C M_{20}} , \tag{22}$$

where C is a geometrical constant of order 10 and d_{SE} is a molecular size. Thus the characteristic wave number k_d is simply related to the molecular size d_{SE},

$$k_d = \left[\frac{3(1-c_0)C}{4} \right]^{1/2} d_{\text{SE}}^{-1} . \tag{23}$$

Estimating $d_{\text{SE}} \simeq \rho_0^{-1/3} = 3.6 \times 10^{-8}$ cm, one obtains $k_d \simeq 7.3 \times 10^7$ cm^{-1}. Since the maximum experimental wave number is much smaller than this, condition (16) is also self-consistent.

The exchange wave number k_e is not well determined in this study because the wave-number range of the data does not extend to sufficiently small values. Good fits to the truncated runs were obtained simply using a constant value of $k_e = 5.2 \times 10^5$ cm^{-1}. Nevertheless, it is interesting to calculate the diffusion coefficient of the modifier $D_{10} = k_B T M_{10}$ using the definition (15) of k_e. The values of $\rho_0^2 \overline{V}_{10}^2 \eta_0$ in Table IV give $D_{10} \simeq 0.6$–3.1×10^{13} cm^2 s^{-1} in the temperature range 950–1014 K. Although no direct diffusivity measurements are available for the composition studied, these values are consistent with oxygen self-diffusion estimates.[35] Oxygen rather than cation diffusion is expected to be the rate-limiting step for diffusion of modifier because of the charge neutrality constraint for the ions. The ratio of k_d^2 to k_e^2 gives a value of $q_m^2 \simeq 5 \times 10^{-5}$, so that the condition (18) is satisfied. One can calculate the ratio of the mobilities to be $M_{20}/M_{10} \simeq 4 \times 10^{-6}$ is this system.

B. Anomalous parameter values near the instability

The material parameters obtained from the DIF theory fits all show interesting behavior near the instability temperature. In Figs. 14–16, it can be seen that $\rho_0 f''(T)$ changes slope, $\rho_0\kappa_0(T)$ peaks, and the deviation of $\rho_0^2\overline{V}_{10}^2\eta_0(T)$ from the estimate increases as the instability is approached. Near the instability temperature, $\rho_0 f''$ is more negative than expected, and $\rho_0\kappa_0$ and $\rho_0^2\overline{V}_{10}^2\eta_0$ are both larger than expected. The directions of these anomalies are related in the same way as the correlations between the sets of parameter values which give good fits to any given data set. In all of the fits, the covariance of $\rho_0\kappa_0$ and $\rho_0^2\overline{V}_{10}^2\eta_0$ is positive, while the covariances of $\rho_0 f''$ with each of the others are negative. This suggests that the anomalies in the parameter values near the instability may be artifacts due to some systematic effect not included in the theory.

One possibility is that nucleated phase separation in the metastable region and similar behavior in the nearby unstable region cause the anomalies. They may also be related to the apparent relaxation of the material parameters with time, as shown in Fig. 13. If the parameters were to continue changing in the same directions for longer times at the lower temperatures, the anomalies would all be reduced.

Another possibility is that nonlinear terms neglected in the DIF theory used above are not negligible and that the good fit of the linearized theory is partly fortuitous. At first sight this seems unlikely, since the scattering data do not show the typical effects of nonlinearity. The overall behavior of the scattering data is in agreement with the basic result of linearized spinodal decomposition theory: The intensity at each wave number changes monotonically in time, relaxing or growing exponentially. In particular, the intensity at higher wave numbers initially increases and relaxes to an Ornstein-Zernike asymptote. Within the time scale of the experiments, the high-wave-number intensity does not begin to decrease, which would produce the "crossing of the tails" typically predicted by nonlinear spinodal decomposition theory[19,22,24] and late-stage coarsening theory. However, some nonlinear-theory results[19] indicate that the "crossing of the tails" is less prominent for an off-critical composition (such as that studied here) than for the critical composition. It may be necessary to take into account nonlinearities to understand the anomalous parameter values near the instability found above. To do this it will be necessary to extend existing nonlinear theories to incorporate the DIF kinetics.

C. Extent of phase separation

The linearization involved in the CHC and DIF theories presented above is expected to be a valid approximation only for systems in which the intermolecular interactions are of sufficiently long range and only at a sufficiently early stage in the phase-separation process.[19–22] Although the conditions on material parameters for the validity of the CHC theory have been considered in some detail, such conditions have yet to be obtained for the flow-limited kinetics of the DIF theory or for off-critical compositions in systems with composition-dependent viscosity and mobilities. Nevertheless, the parameter values obtained from the DIF theory fits suggest that the time range of this experiment is within the early-stage regime. At all temperatures the maximum value of the amplification factor $R(k)$ is less than 10^{-4} s^{-1}, so that the experimental times are all significantly smaller than the exponential time constant $(2R)^{-1}$ of the most unstable fluctuations.

The extent of phase separation can be estimated in a manner independent of spinodal decomposition theory by standard analyses of the small-angle scattering data. In the late stage of phase separation, the phase boundaries are expected to be sharp relative to the domain size of the two-phase structure. The structure factor then has a characteristic k^{-4} dependence at higher wave numbers (Porod's law).[42] Figure 17 shows structure factors for several temperatures plotted versus wave number on logarithmic scales. The data points are the same as those shown in Fig. 9, and the lines are the same Ornstein-Zernike asymptotes shown there. One can see that the slope at higher wave numbers does not have the Porod-law value, indicating that the phase boundaries remain relatively diffuse throughout the times studied here.

One commonly used measure of the extent of phase separation is the mean-square composition deviation $\langle(\Delta c)^2\rangle$. This can be obtained from the integral of the structure factor by the relation

$$\langle(\Delta c)^2\rangle(t)\equiv\frac{1}{V}\int_V[c(\mathbf{r},t)-c_0]^2 d\mathbf{r} = \frac{1}{8\pi^3}\int_0^\infty \hat{S}(k,t)4\pi k^2 dk \ . \tag{24}$$

The mean-square composition deviation is expected to approach a constant value $\langle(\Delta c)^2\rangle_{\rm eq}$ during the late

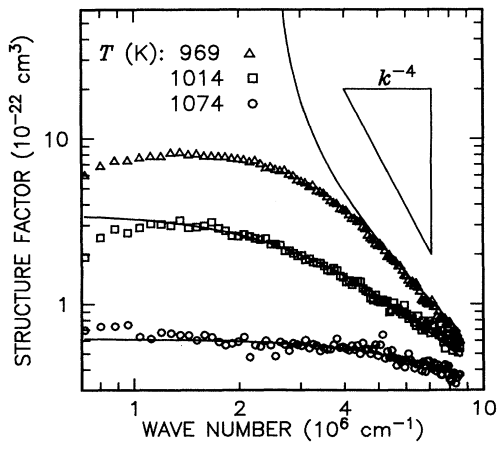

FIG. 17. Plot of structure factors from several temperatures as a function of wave number on logarithmic scales, showing that the high-wave-number tails do not obey Porod's law. Solid lines: Ornstein-Zernike asymptotes from Fig. 9.

stage of phase separation, when the system consists of fixed volume fractions of the two coexisting phases. Figure 18 shows the evaluation of $\langle(\Delta c)^2\rangle(t)$ from data at each temperature studied. The graphs on the left show the integrand of Eq. (24) as a function of wave number at various times. Values of $\hat{S}(k,t)$ for the points shown have been obtained by adding the fit to run Z used for $\hat{S}(k,0)$ to the measured values of $\Delta\hat{S}(k,t)$. The solid line is the contribution from $\hat{S}(k,0)$. Since data are not available for all wave numbers, the integral of the structure factor in Eq. (24) can be evaluated directly only between low- and high-wave-number limits $k_{\min}$ and $k_{\max}$. One can see that, although the error in the integral due to the lack of data at small wave numbers is minimal, the value of the integral will depend strongly on the value chosen for $k_{\max}$. The graphs on the right show the integral as a function of time calculated using two values of $k_{\max}$. In both cases the low-wave-number limit used is at the edge of the measured data, $k_{\min}\simeq 0.7\times 10^6$ cm^{-1}. The solid symbol at zero time represents the integral of the initial state $\hat{S}(k,0)$. At the three lower temperatures, the integral continues to grow with time throughout the measurement, indicating that the late stage has not been reached. At the highest temperature, the integral saturates during the time of the observation. In the linearized theory, this is interpreted as the equilibration of fluc-

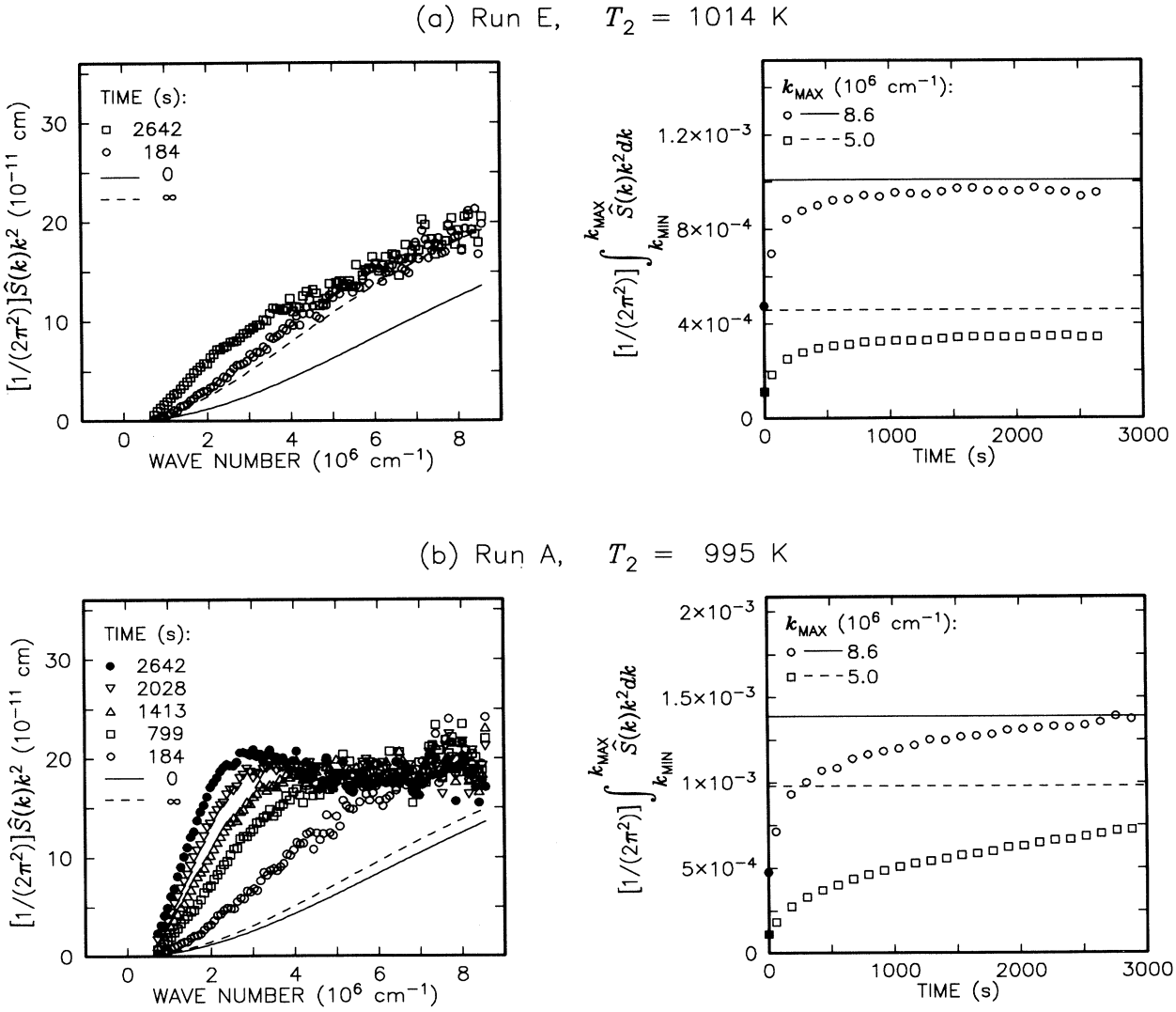

FIG. 18. Evaluation of integrated structure factor for runs at each temperature. Graphs of both the integrand as a function of wave number at several times and the integral as a function of time are shown for each run. On the graphs of the integrand, the contributions from $\hat{S}(k,0)$ are shown as solid lines. Late-stage values estimated from the regular solution model are shown as dashed lines on the integrand graphs and as solid and dashed lines on the integral graphs. The integrals are presented for two values of $k_{\max}$.

tuations in the metastable region above the spinodal, rather than the true equilibration to a two-phase structure.

For comparison, values of $\langle(\Delta c)^2\rangle_{eq}$ can be calculated for a late-stage two-phase system by considering the contributions from the average composition and the fluctuations in each phase:

$$\langle(\Delta c)^2\rangle_{eq}=\phi[(c_\alpha-c_0)^2+\langle(c-c_\alpha)^2\rangle_\alpha] +(1-\phi)[(c_\beta-c_0)^2+\langle(c-c_\beta)^2\rangle_\beta] . \quad (25)$$

Here c_α and c_β are the average compositions of the two coexisting phases α and β, respectively, ϕ is the volume fraction of the α phase, and the second term in each square bracket is the mean-square deviation about the average composition in each phase due to equilibrium thermal fluctuations. In analogy with Eq. (24) for the complete two-phase system, the equilibrium mean-square deviation within either phase can be written as

$$\langle(c-c_\alpha)^2\rangle_\alpha=\frac{1}{8\pi^3}\int_0^\infty \hat{S}_\alpha(k)4\pi k^2\,dk , \quad (26)$$

where $\hat{S}_\alpha(k)$ is the equilibrium structure factor in that phase, relative to its average composition c_α. Values of c_α, c_β, $\hat{S}_\alpha(k)$, $\hat{S}_\beta(k)$, and ϕ can be obtained from the regular solution model (see Appendix). These calculations show that the contribution to $\langle(\Delta c)^2\rangle_{eq}$ from equilibrium fluctuations can be larger than that from the average composition of a phase. The resulting values are shown

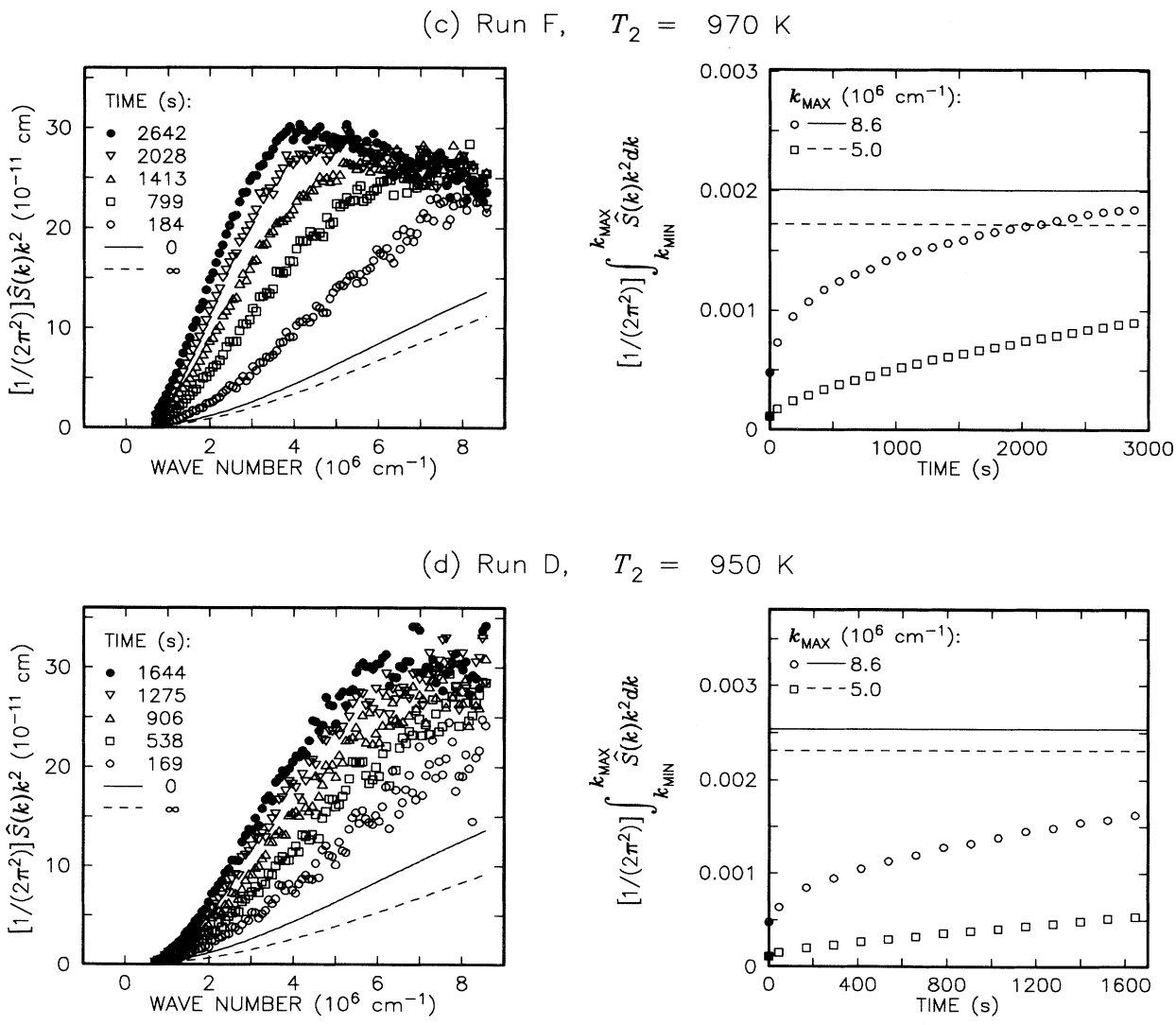

FIG. 18. (*Continued*).

in the graphs on the right in Fig. 18. Although reasonable agreement is obtained between these values and the trend of the integrated scattering data, caution is required in using this comparison to estimate the extent of phase separation because of the fluctuation contributions and the $k_{\max}$ dependence. For example, $\langle(\Delta c)^2\rangle(t)$ does not necessarily grow monotonically with time, but could exceed $\langle(\Delta c)^2\rangle_{\rm eq}$ at some intermediate time, particularly for large values of $k_{\max}$.

It is also instructive to compare the measured structure factors to an estimate of the eventual equilibrium structure factor of the two-phase system, $\hat{S}_{\rm eq}(k)$. This can likewise be calculated by considering the average composition and the fluctuations in each phase:

$$\hat{S}_{\rm eq}(k)=\phi[(c_\alpha-c_0)^2 8\pi^3\delta^3(k)+\hat{S}_\alpha(k)] +(1-\phi)[(c_\beta-c_0)^2 8\pi^3\delta^3(k)+\hat{S}_\beta(k)] \ . \quad (27)$$

At very long times, the scattering from the coarsened two-phase domains will have collapsed to a δ function at zero wave number, and the remaining scattering will be from the equilibrium fluctuations in each phase. This late-time limit, calculated from the regular solution model, is shown as a dashed line on each graph on the left of Fig. 18. One can see that the measured structure factors grow towards an asymptote that is significantly higher than $\hat{S}_{\rm eq}(k)$, indicating that the observed exponential relaxation is not simply the attainment of the final equilibrium structure.

D. Material parameter drift due to structural relaxation

The apparent changes in fit parameter values with time following the quench (as shown in Fig. 13) can be attributed to structural relaxation, a generic feature of glassy systems. This interpretation is suggested by the larger amplitude changes found for deeper quenches. Effects of structural relaxation on material parameters have been considered in previous analyses of spinodal decomposition in glass-forming oxides.[17,43,44] In those analyses, large structural relaxation effects were invoked to explain the large discrepancies between the experimental data and the CHC theory. In the present study, a much smaller effect would explain a much smaller discrepancy between the data and the DIF theory. Since the effect of structural relaxation on material parameters in glassy systems is poorly understood, unequivocal analysis of the kinetics of any process following a quench is not possible. The relatively shallow quenches used in this study should tend to reduce any structural relaxation effects.

The DIF theory suggests that the time scale for structural relaxation in glassy systems may often be similar to that for spinodal decomposition or other interdiffusion processes at small length scales. When the components have very different mobility, DIF theory predicts that viscous flow is the rate-limiting step for interdiffusion over length scales smaller than k_e^{-1}. Thus diffusion of the slowest species (e.g., the network) over molecular length scales gives the time scale for both structural relaxation and interdiffusion, making it difficult to ever observe the effects of each process separately.

E. Generality of results

The structure factors observed in this study all have a characteristic asymmetric peak shape, wider on the high-wave-number side than the low-wave-number side, and the position of the peak remains relatively constant during each run. Such behavior has also been found in all previous small-angle x-ray-scattering studies of spinodal decomposition in amorphous oxides.[4–7,11,17] Since this behavior is reproduced by the kinetic equation of the DIF theory (but not that of the CHC theory), it is likely that the DIF kinetics are applicable to all of the previous data. The systems used in all of these studies have a large difference between the mobilities of the diffusing species, since they all phase separate into network- and modifier-rich amorphous phases. This is consistent with the DIF theory result which explains the behavior, i.e., that viscous flow is the rate-limiting step for interdiffusion at small length scales when there is a large difference between the mobilities. In contrast, studies of spinodal decomposition in metal alloys in which the mobilities do not differ[45] typically find a symmetric peak in the structure factor which shifts with time, consistent with nonlinear extensions to the CHC theory.

The generality of the present results should be tested by future studies which include longer times and compositions closer to the critical composition. Improved techniques will make possible similar studies of other amorphous oxide systems such as SiO_2-Na_2O. The predictions of the DIF theory could be tested further by a comparative study of the SiO_2-B_2O_3-Na_2O system, in which the mobilities are not expected to differ as much because phase separation occurs between two network formers. The theory should also be applied to studies of spinodal decomposition in polymer systems.[46] The conclusion that viscous flow can control the kinetics of spinodal decomposition through the DIF mechanism has wide-ranging consequences for the kinetics of other processes such as nucleated phase separation, crystallization, and interdiffusion in thin films or surface layers. Measurements of composition profiles during the interdiffusion of thin layers would be a direct test of this result.

V. CONCLUSIONS

Our ability to measure the small-angle x-ray scattering in real time following direct quenches from the single-phase region allowed us to study the early stage of phase separation in an important range of temperatures: in both the metastable and unstable regions, and both above and below the maximum in the phase-separation rate. While the scattering data agree qualitatively with the linearized thermodynamics of the CHC theory (i.e., the structure factor changes exponentially with time at each wave number), the wave-number dependence of the amplification factor does not agree with the simple diffusive kinetics used in the CHC theory. Instead, quantitative agreement is found at each temperature using the kinetics of the DIF theory for interdiffusion,[28] giving reasonable values of the material parameters $\rho_0 f''$, $\rho_0\kappa_0$, and $\rho_0^2\bar{V}_{10}^2\eta_0$ as a function of temperature. The results of

this study of spinodal decomposition indicate that deformation to relax stress may be the rate-limiting step for any process involving short-distance interdiffusion of network-forming and network-modifying species.

ACKNOWLEDGMENTS

The authors would like to thank Carol Thompson, Stephen Laderman, Michael Moldover, and John Cahn for illuminating discussions. We are grateful to Judith Roldan for carrying out the viscosity measurements and to Dale Kauffman for preparing the glasses. This work was supported in part by National Science Foundation (NSF) Grant No. DMR79-08554. G.B.S. was supported in part by the Fannie and John Hertz Foundation. At the time of the experimental part of this work, W.K.W. was a staff member at Stanford Synchrotron Radiation Laboratory (SSRL). A part of this work was carried out at SSRL, which was supported by the National Science Foundation.

APPENDIX

The miscibility gap in the SiO_2-BaO-K_2O system is well described by a pseudobinary regular solution model.[25,30–33] This model is used to calculate the phase diagrams shown in Figs. 1 and 2. The molecular units and interaction energies used in the regular-solution model are chosen to agree with data for the SiO_2-BaO and SiO_2-K_2O systems and with one measured ternary immiscibility temperature[30] (which happens to be for the composition studied here). For the pseudobinary section of interest here, the composition is expressed in terms of these molecular units by

$$N(18SiO_2)_{1-\gamma}\, N(7SiO_2\cdot BaO\cdot K_2O)_{\gamma} , \tag{A1}$$

where γ is the composition variable and N is a constant giving the absolute size of the units. The relationship between the mole fractions γ and c of expressions (A1) and (1), respectively, is

$$\gamma=\frac{18c}{2+9c} . \tag{A2}$$

The free energy per molecule of the units given in expression (A1) is given by

$$f_\gamma=k_BT[\gamma\ln\gamma+(1-\gamma)\ln(1-\gamma)]+2k_BT_c\gamma(1-\gamma) , \tag{A3}$$

where $T_c=1042$ K is the critical temperature in the pseudobinary section. From this one can obtain the immiscibility temperature

$$T_{\rm imm}=\frac{2(1-2\gamma)}{\ln[(1-\gamma)/\gamma]}T_c \tag{A4}$$

and the mean-field spinodal temperature

$$T_s=4\gamma(1-\gamma)T_c . \tag{A5}$$

If the pseudobinary miscibility gap of Fig. 2 were replotted using the composition variable γ, it would be symmetric with a critical point at $\gamma=\frac{1}{2}$. The composition studied ($c_0=0.10$) corresponds to the off-critical composition $\gamma_0=0.62$. These equations give $T_{\rm imm}=1021$ K and $T_s=981$ K for this composition.

The regular solution model can be used to estimate values of $\rho_0 f''$ as a function of temperature for comparison with the experimental values. The second derivative of the free energy per mole f_γ with respect to composition γ can be calculated from Eq. (A3):

$$\frac{d^2f_\gamma}{d\gamma^2}=\frac{k_B(T-T_s)}{\gamma(1-\gamma)} . \tag{A6}$$

This quantity is proportional to $T-T_s$ with a temperature derivative determined by the configurational entropy term in Eq. (A3). The free energy per molecule used in the data analysis differs from that used in the regular-solution model because the molecules are defined using expression (1) rather than expression (A1). These molecular free energies are related by

$$f_\gamma=\frac{36N}{2+9c}f . \tag{A7}$$

Likewise, molecular densities ρ and ρ_γ defined using the units in expressions (1) and (A1), respectively, are related by

$$\rho_\gamma=\frac{2+9c}{36N}\rho . \tag{A8}$$

One can then show that the free-energy curvatures are related by

$$\rho_\gamma\frac{d^2f_\gamma}{d\gamma^2}=\left[\frac{dc}{d\gamma}\right]^2\rho\frac{d^2f}{dc^2} , \tag{A9}$$

where the derivative of the two composition variables is given by

$$\frac{dc}{d\gamma}=\frac{(2+9c)^2}{36} . \tag{A10}$$

Using the definition (10) of f'', the regular solution result (A6), and relations (A2) and (A8)–(A10) between the composition variables, one obtains

$$\rho_0f''=\frac{2\rho_0k_B(T-T_s)}{Nc_0(2+9c_0)(2-9c_0)} . \tag{A11}$$

The regular-solution model thus predicts that $\rho_0 f''$ is proportional to $T-T_s$ and that its temperature derivative is inversely proportional to the size N of the molecular units.

The regular solution model can be used to calculate the compositions, volume fractions, and equilibrium structure factors of each phase which enter into $\langle(\Delta c)^2\rangle_{\rm eq}$ and $\hat{S}_{\rm eq}(k)$. The average compositions c_α and c_β are obtained by inverting Eqs. (A4) and (A2). The volume fraction depends on the densities of the two phases. For small density differences, it is given by

$$\phi\simeq\frac{c_\beta-c_0}{c_\beta-c_\alpha}\left[1+\frac{1}{\rho}\frac{d\rho}{dc}(c_0-c_\alpha)\right] , \tag{A12}$$

using a value of $1/\rho\, d\rho/dc=0.12$. The equilibrium structure factors can be evaluated using the Ornstein-Zernike form

$$\hat{S}_\alpha(k)=\frac{k_B T}{[\rho(d^2 f/dc^2)(1+\xi^2 k^2)]_{c=c_\alpha}} , \tag{A13}$$

where ξ is the correlation length, and the denominator is to be evaluated at c_α. It is convenient to use the expression

$$\xi^2 \equiv \frac{2\kappa}{d^2 f/dc^2}=\frac{2\kappa_\gamma}{d^2 f_\gamma/d\gamma^2} , \tag{A14}$$

where κ_γ is the gradient energy coefficient defined using the regular-solution molecular units of expression (A1). Like ξ and $d^2 f_\gamma/d\gamma^2$, its values in the two coexisting phases are equal. It is related to κ by

$$\kappa_\gamma=\frac{(2+9c)^3 N}{36}\kappa . \tag{A15}$$

To evaluate ξ, the same value of $\kappa_\gamma=3.4\times10^{-28}$ erg cm^2 was used at each temperature, obtained from the value of $\rho_0\kappa_0$ in Table II. The estimates of $\langle(\Delta c)^2\rangle_{\rm eq}$ and $\hat{S}_{\rm eq}(k)$ shown in Fig. 18 involve significant uncertainty because of the number of approximations used, such as the assumption that the value $d\rho^e/dc$ relating the structure factor to the scattering cross section is constant over the two-phase region.

[1]J. W. Cahn, Acta Metall. **9**, 795 (1961).
[2]L. S. Darken, Trans. Metall. Soc. AIME **175**, 184 (1948).
[3]G. F. Neilson, Phys. Chem. Glasses **10**, 54 (1969).
[4]J. Zarzycki and F. Naudin, J. Non-Cryst. Solids **1**, 215 (1969).
[5]N. S. Andreev, G. G. Boiko, and N. A. Bokov, J. Non-Cryst. Solids **5**, 41 (1970).
[6]N. S. Andreev and E. A. Porai-Koshits, Discuss. Faraday Soc. **50**, 135 (1970).
[7]M. Tomozawa, R. K. MacCrone, and H. Herman, Phys. Chem. Glasses **11**, 136 (1970).
[8]J. Zarzycki and F. Naudin, J. Non-Cryst. Solids **5**, 415 (1971).
[9]G. R. Srinivasan, R. Collela, P. B. Macedo, and V. Volterra, Phys. Chem. Glasses **14**, 90 (1973).
[10]M. Roth and J. Zarzycki, J. Non-Cryst. Solids **16**, 93 (1974).
[11]A. F. Craievich, Phys. Chem. Glasses **16**, 133 (1975).
[12]R. J. Acuna and A. F. Craievich, J. Non-Cryst. Solids **34**, 13 (1979).
[13]A. F. Craievich and J. R. Olivieri, J. Appl. Crystallogr. **14**, 444 (1981).
[14]C. M. Jantzen, D. Schwahn, J. Schelten, and H. Herman, Phys. Chem. Glasses **22**, 122 (1981); **22**, 138 (1981).
[15]A. Craievich and J. M. Sanchez, Phys. Rev. Lett. **47**, 1308 (1981).
[16]S. Bras *et al.*, Nucl. Instrum. Methods **208**, 489 (1983).
[17]R. Yokota and H. Nakajima, J. Non-Cryst. Solids **70**, 343 (1985).
[18]A. F. Craievich, J. M. Sanchez, and C. E. Williams, Phys. Rev. B **34**, 2762 (1986).
[19]J. S. Langer, M. Bar-On, and H. D. Miller, Phys. Rev. A **11**, 1417 (1975).
[20]K. Binder, Phys. Rev. A **29**, 341 (1984).
[21]D. W. Heermann, Phys. Rev. Lett. **52**, 1126 (1984).
[22]M. Grant, M. San Miguel, J. Vinals, and J. D. Gunton, Phys. Rev. B **31**, 3027 (1985).
[23]H. E. Cook, Acta Metall. **18**, 297 (1970).
[24]J. S. Langer, Acta Metall. **21**, 1649 (1973).
[25]G. B. Stephenson, Ph.D. dissertation, Stanford University, 1983.
[26]G. B. Stephenson, J. Non-Cryst. Solids **66**, 393 (1984).
[27]G. B. Stephenson, Scr. Metall. **20**, 465 (1986).
[28]G. B. Stephenson, Acta. Metall. **36**, 2663 (1988).
[29]P. F. James, J. Mater. Sci. **10**, 1802 (1975).
[30]Y. Kawamoto and M. Tomozawa, J. Am. Ceram. Soc. **64**, 289 (1981).
[31]W. Haller, D. H. Blackburn, and J. H. Simmons, J. Am. Ceram. Soc. **57**, 120 (1974).
[32]Y. Kawamoto and M. Tomozawa, Phys. Chem. Glasses **22**, 11 (1981).
[33]Z. Strnad, J. Non-Cryst. Solids **38**, 711 (1980).
[34]J. E. Morral and J. W. Cahn, Acta Metall. **19**, 1037 (1971).
[35]G. H. Frischat, *Ionic Diffusion in Oxide Glasses* (Trans Tech, Bay Village, OH, 1975).
[36]N. G. Webb *et al.*, Rev. Sci. Instrum. **47**, 836 (1976); N. G. Webb, *ibid.* **47**, 545 (1976).
[37]B. E. Warren, *X-ray Diffraction* (Addison-Wesley, Reading, MA, 1969).
[38]J. W. Cahn and J. E. Hilliard, J. Chem. Phys. **28**, 258 (1958); **31**, 688 (1959).
[39]J. S. Langer, Ann. Phys. (N.Y.) **65**, 53 (1971); J. S. Langer and M. Bar-On, *ibid.* **78**, 421 (1973).
[40]L. S. Ornstein and F. Zernike, Proc. Acad. Sci. Amsterdam **17**, 793 (1914).
[41]P. R. Bevington, *Data Reduction and Error Analysis for the Physical Sciences* (McGraw-Hill, New York, 1969).
[42]G. Porod, in *Small-Angle X-ray Scattering,* edited by O. Glatter and O. Kratky (Academic, London, 1982).
[43]A. F. Craievich, Phys. Status Solidi A **28**, 609 (1975).
[44]R. Yokota, J. Phys. Soc. Jpn. **45**, 29 (1978).
[45]See, e.g., J. J. Hoyt *et al.*, Acta Metall. **37**, 1597 (1989).
[46]See, e.g., T. Sato and C. C. Han, J. Chem. Phys. **88**, 2057 (1988).